Tectonophysics 871 (2024) 230175

Contents lists available at ScienceDirect

Tectonophysics

journal homepage: www.elsevier.com/locate/tecto

Inverse magnetic fabric of remagnetized limestones in the Zaduo area, Eastern Qiangtang Terrane: Implications for oroclinal bending in the Eastern Himalayan Syntaxis

Qiang Fu [a,b], Maodu Yan [a,c,*], Mark J. Dekkers [b], Bingshuai Li [d], Chong Guan [e], Liang Yu [f], Wanlong Xu [a,c], Miaomiao Shen [a], Zunbo Xu [a,c]

[a] State Key Laboratory of Tibetan Plateau Earth System, Resources and Environment (TPESRE), Institute of Tibetan Plateau Research, Chinese Academy of Sciences, Beijing 100101, China
[b] Department of Earth Sciences, Paleomagnetic Laboratory 'Fort Hoofddijk', Utrecht University, Budapestlaan 17, Utrecht 3584 CD, the Netherlands
[c] University of Chinese Academy of Sciences, Beijing 100049, China
[d] School of Earth Sciences, East China University of Technology, Nanchang 330013, China
[e] Xi'an Center of Geological Survey (Northwest China Center of Geoscience Innovation), China Geological Survey, Xi'an 710054, China
[f] School of Ecology, Resources and Environment, Dezhou University, Dezhou 253023, China

A R T I C L E I N F O

Keywords:
Inverse magnetic fabric
Remagnetization
Rock magnetism
Eastern Qiangtang Terrane
Tibetan Plateau

A B S T R A C T

Magnetic fabric analysis is a common technique to assess the strain regime during mountain building processes. Here, we use this approach to evaluate the tectonic evolution of the Tibetan Plateau and the Eastern Himalayan Syntaxis by analyzing the limestones of the Jurassic Buqu Formation in the Zaduo area, Eastern Qiangtang Terrane (China). These limestones were chemically remagnetized during the Cenozoic. For a proper assessment, it is relevant to understand how the mineralogy of the remagnetized limestones affects their magnetic fabric and how the magnetic fabric can improve our understanding of the tectonic strain and regional deformation. The role of the authigenic magnetite in the development of the magnetic fabric should thus be explored. Comparison of the bulk susceptibility (K_m) with various natural and laboratory rock magnetic properties (K_m versus natural remanent magnetization, K_m versus saturation isothermal remanent magnetization, and K_m versus saturation magnetization) indicates that susceptibility and remanences are both carried by authigenic magnetite. Most of the magnetite grains show axial ratios <1.3:1 according to the Néel diagram, and fall within the single-domain range based on the mass magnetic susceptibility (χ) and DC field-normalized anhysteretic remanent magnetization (χ_{ARM}) ratio, giving rise to the inverse magnetic fabric observed. Twelve sites (120 specimens) are divided into four groups based on the magnetic fabric and rock magnetic behaviors. Overall, there is a clear trend of decreasing K_m, natural remanent magnetization, saturation isothermal remanent magnetization, ferromagnetic percentage and shape parameter from Group I to IV. The K_1 axis of all four groups documents a NNE-SSW oriented compression during remagnetization, contrasting with the Eocene NE-SW compression in the Gongjue area farther east. This different compressional regime likely resulted in different rotations and structural trends surrounding the Eastern Himalayan Syntaxis.

1. Introduction

The Tibetan Plateau is commonly seen as a key natural laboratory for studying geodynamic processes of intra-continental collision and their impacts on paleoclimate change, biodiversity evolution, and mineral resource enrichment (Molnar and Tapponnier, 1975; An et al., 2001; Tapponnier et al., 2001; Hou et al., 2007; Royden et al., 2008; Yan et al., 2016; Su et al., 2020). It is composed of multiple terranes that amalgamated prior to the early Cenozoic, and the India-Eurasia collision is a critical player in the uplift and growth of the Tibetan Plateau (Molnar and Tapponnier, 1975; Burchfiel et al., 1989; England and Houseman, 1989; Royden et al., 1997; Yin and Harrison, 2000; Tapponnier et al.,

* Corresponding author at: State Key Laboratory of Tibetan Plateau Earth System, Resources and Environment (TPESRE), Institute of Tibetan Plateau Research, Chinese Academy of Sciences, Beijing 100101, China.
E-mail address: maoduyan@itpcas.ac.cn (M. Yan).

https://doi.org/10.1016/j.tecto.2023.230175
Received 17 May 2023; Received in revised form 11 December 2023; Accepted 12 December 2023
Available online 15 December 2023

2001; Wang et al., 2008; Zhang et al., 2020). Issues directly associated with the India-Eurasia collision include the uplift and deformation of the Tibetan Plateau (England and Houseman, 1989; Royden et al., 1997; Tapponnier et al., 2001; Wang et al., 2008; Ding et al., 2022), regional or even global climate change associated with this collision (e.g., Ruddiman and Kutzbach, 1989; Raymo and Ruddiman, 1992; Fang et al., 2016; Wu et al., 2022), and the enrichment of mineral resources (Hou et al., 2007; Hou and Zhang, 2015). As the prime driver of the uplift and growth of the Tibetan Plateau, the northward indentation and subsequent subduction of the Indian Plate underneath the Eurasian Plate have resulted in widespread lithospheric crustal shortening and extrusion in Asia (Molnar and Tapponnier, 1975; Burchfiel et al., 1989; Yang and Besse, 1993; Chen et al., 1995; Beck et al., 1995; Yin and Harrison, 2000; Replumaz and Tapponnier, 2003; van Hinsbergen et al., 2011; Chen et al., 2015), and clockwise rotation around the Eastern Himalayan Syntaxis (EHS) in the southeastern Tibetan Plateau (Yang et al., 2001; Sato et al., 2007; Tanaka et al., 2008; Kondo et al., 2012; Tong et al., 2013; Kornfeld et al., 2014; Gao et al., 2015; Li et al., 2017; Tong et al., 2017). The widespread rotation and southeastward extrusion of the southeastern Tibetan Plateau are believed to be associated with lithospheric-scale strike-slip fault systems (Gao et al., 2015; Leloup et al., 1995; Li et al., 2017; Sato et al., 2007; Tapponnier et al., 1990; Tong et al., 2013), and/or uplift of the southeastern Tibetan Plateau (Hoke et al., 2014; Li et al., 2019; Su et al., 2019; Tang et al., 2017; Xiong

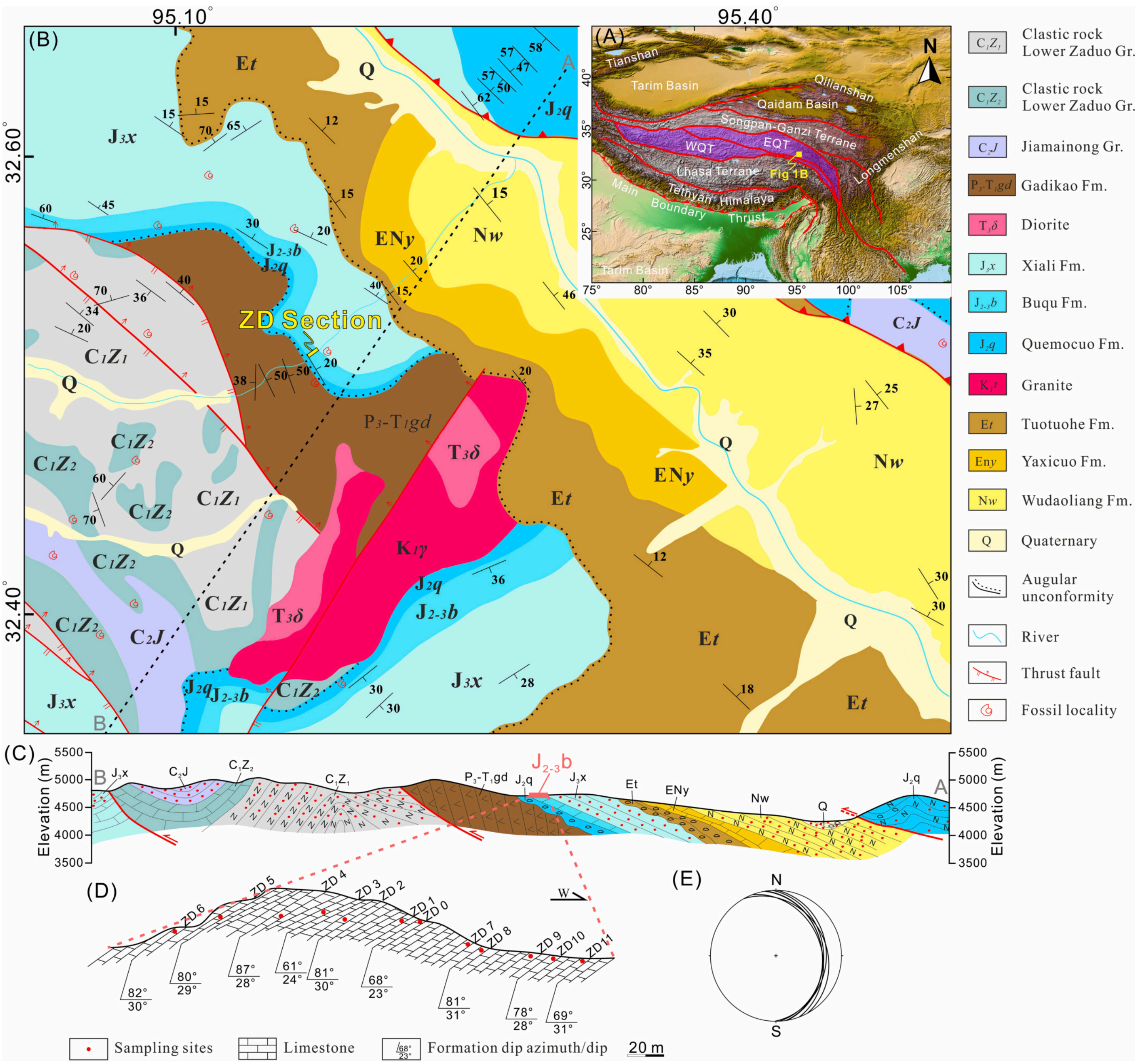

Fig. 1. (A) Topographic map of the Tibetan Plateau and surrounding areas; the red lines outline major suture zones. The abbreviations of the tectonic units are EQT: Eastern Qiangtang Terrane; WQT: Western Qiangtang Terrane. (B) Geological map of the Zaduo area showing the location of the sampled succession; the black dashed line AB represents the cross-section of the Zaduo area (Qinghai Geological Survey Institute (QGSI), 2014) displayed in (C). (C) Cross-section AB showing the exposed sedimentary succession. (D) Cross-section showing the sampling sites. Note: the sampled section is not on the cross-section AB, but it is in the same stratigraphic position as the pink horizontal bar marked in (C). (E) Equal-area lower-hemisphere stereographic projection of the bedding attitudes. (B) and (D) are modified from Fu et al. (2022). (For interpretation of the references to colour in this figure legend, the reader is referred to the web version of this article.)

et al., 2020).

The main part of the Tibetan Plateau consists of, from north to south, the Songpan-Ganzi, Qiangtang and Lhasa terranes. The Qiangtang Terrane, situated in the central Tibetan Plateau (Fig. 1A), is separated geologically from the Songpan-Ganzi Terrane by the Jinshajiang suture zone to the north and from the Lhasa Terrane by the Bangong-Nujiang suture zone to the south. It is further divided into the Eastern (also referred to as Northern) Qiangtang Terrane (EQT) and the Western (or Southern) Qiangtang Terrane by the Longmu Co-Shuanghu suture zone (Fig. 1A; Li, 1987; Huang et al., 1992; Yin and Harrison, 2000; Pan et al., 2004; Li et al., 2009; Metcalfe, 2013; Zhu et al., 2013, 2016; Yan et al., 2016). The easternmost part of the Qiangtang Terrane is a transitional area adjacent to the southeastern Tibetan Plateau. Therefore, knowledge on the post-collisional deformation of the EQT will enhance our understanding of the rotational history and southeastward extrusion in the southeastern Tibetan Plateau. Several paleomagnetic studies have been carried out on Cenozoic strata in the EQT to constrain its paleolatitude and quantify vertical axis rotations (Lippert et al., 2011; Roperch et al., 2017; Tong et al., 2017; Zhang et al., 2018, 2020; Li et al., 2020b). These studies provide solid tectonic evidence for various deformation and uplift scenarios. Despite its effectiveness for tectonic strain analysis in structural geology, magnetic fabric analysis is rather uncommon in this region.

Many previous studies have demonstrated that anisotropy of magnetic susceptibility (AMS, also termed magnetic fabric), is a swift and powerful tool, which can provide essential insight into basin evolution (e.g., Mattei et al., 1997; Cifelli et al., 2005; Oliva-Urcia et al., 2010, 2011, 2013; Yu et al., 2014; Tang et al., 2015; Li et al., 2020a, 2020c, 2021; Jiang et al., 2022), emplacement of igneous bodies (e.g., Hrouda, 1982; Bascou et al., 2005; Antolín-Tomás et al., 2009; Cañón-Tapia and Mendoza-Borunda, 2014; Yan et al., 2019), fold/fault deformation (e.g., Aubourg et al., 1999; Saint-Bezar et al., 2002; Evans et al., 2003; Luo et al., 2009; García-Lasanta et al., 2015), and paleocurrent directions (e.g., Tarling and Hrouda, 1993; Pueyo Anchuela et al., 2013; Ejembi et al., 2020; Bilardello, 2021). A fundamental step prior to interpreting AMS data is to ascertain what minerals give rise to magnetic fabric. Recently, a paleomagnetic study with detailed rock magnetic experiments was conducted on Jurassic limestones from the EQT, where authigenic magnetite was responsible for the Cenozoic secondary remanent magnetization (Fu et al., 2022). This provides a good opportunity to explore how the characteristic mineralogy of remagnetized limestones, which contain large amounts of superparamagnetic (SP) and stable single domain (SD) magnetite, affects the AMS, and how this magnetic fabric can shed light on the tectonic strain and regional deformation. Thus, we compare relations between AMS and various rock magnetic properties, including natural remanent magnetization (NRM), saturation isothermal remanent magnetization (SIRM), and saturation magnetization (M_s). Additionally, we propose the prevalence of an inverse magnetic fabric in these remagnetized limestones. The obtained results are of interest for the compression and deformation history of the east central Tibetan Plateau in response to the early India-Eurasia collision.

2. Geological setting

Our study area, the Zaduo area, has an average elevation of ~4700 m (Fig. 1C) and lies in a transitional region of the EQT. In this region, the structural orientations gradually shift from east-west in the western part of EQT to north-south in the eastern part (Fig. 1A). The tectonic lineaments (e.g., faults and fold axial planes) in the Zaduo area are NW-SE oriented (Fig. 1B), in accordance with the regional trending of the east central Qiangtang Terrane (Fig. 1A, Qinghai Geological Survey Institute (QGSI), 2014). These tectonic features are mostly associated with the significant Cenozoic shortening and strike-slip faulting in response to the India-Eurasia collision (Horton et al., 2002; Kapp et al., 2005).

Paleozoic to Cenozoic rocks are exposed in the Zaduo area (Fig. 1B, refer to Fu et al., 2022 for more detailed descriptions). Our target rocks, the limestones of the Middle-Upper Jurassic Buqu Formation, were collected from a monoclinal succession. Previous high-resolution magnetostratigraphic studies were conducted in the Yanshiping area (~300 km to the west of the Zaduo area) and constrained the Buqu Formation to be ~165.5 Ma–163.3 Ma (Fang et al., 2016; Song et al., 2016; Yan et al., 2016). The AMS sites studied in this contribution were paleomagnetically investigated before and deemed to be remagnetized, as testified by rock magnetic investigations and petrographic observations (Fu et al., 2022). The co-occurrence of SP and stable SD magnetite in these rocks generates 'wasp-waisted' hysteresis loops and hysteresis parameters plot on the 'remagnetization trend' in the Day plot (Fu et al., 2022). The oxidation of existing iron sulfides to authigenic magnetite was argued to be a major magnetization mechanism (Fu et al., 2022). Additionally, the declination, paleolatitude, and paleopoles calculated from the sites are consistent with those obtained from previous paleomagnetic studies on Paleogene/Eocene rocks (Fu et al., 2022). The acquisition of the secondary NRM was dated to the Paleogene, most likely to the Eocene (Fu et al., 2022).

3. Applied techniques

AMS is a second-rank symmetrical tensor that can be graphically displayed by an ellipsoid with orthogonal principal axes that represent the three principal magnetic susceptibilities, namely: K_1 (maximum), K_2 (intermediate), and K_3 (minimum) (e.g., Tarling and Hrouda, 1993). Magnetic lineation L (K_1/K_2) and foliation F (K_2/K_3) are often used to characterize the magnetic ellipsoids. Additionally, other essential AMS parameters, including mean magnetic susceptibility (K_m), the corrected degree of anisotropy (P_j) and the shape parameter (T) are defined as follows:

$$Km = \frac{K_1 + K_2 + K_3}{3}$$

$$Pj = exp\sqrt{2\left[(\eta_1 - \eta_m)^2 + (\eta_2 - \eta_m)^2 + (\eta_3 - \eta_m)^2\right]}$$

$$T = \left[\frac{2ln(K_2/K_3)}{ln(K_1/K_3)}\right] - 1$$

where $\eta_1 = \ln K_1$, $\eta_2 = \ln K_2$, $\eta_3 = \ln K_3$, and $\eta_m = (\eta_1 + \eta_2 + \eta_3)/3$ (Jelínek, 1977; Jelinek, 1981; Jelínek and Kropáček, 1978). P_j is associated with lithostratigraphic variations and strain (Hrouda, 1982) and typically does not exceed 1.1 in sedimentary rocks (Tarling and Hrouda, 1993). A negative value for T ($-1 < T < 0$) is indicative of a prolate ellipsoid, whereas a positive T ($0 < T < 1$) corresponds to an oblate ellipsoid.

Magnetic susceptibility measurements were performed using a MFK1-FA Kappabridge susceptometer (AGICO Inc., Brno, Czech Republic) at room temperature with an applied magnetic field of 300 A/m and frequency of 976 Hz. The measurements took place at the paleomagnetic laboratory of the State Key Laboratory of Tibetan Plateau Earth System, Resources and Environment (TPESRE), Institute of Tibetan Plateau Research, Chinese Academy of Sciences (ITPCAS, Beijing, China). AMS data were processed using the Anisoft 4.2 and Anisoft 5.0 software packages (Chadima and Jelinek, 2009), and Stereonet 11 software (Allmendinger et al., 2011; Cardozo and Allmendinger, 2013) was employed for plotting.

NRM measurements were conducted with a superconducting quantum interference device (SQUID) magnetometer (2G Enterprises) hosted in a magnetically shielded room (<170 nT). SIRM was determined in an applied magnetic field of 1000 mT with a Lakeshore 8600 Vibrating Sample Magnetometer (VSM). Magnetization versus temperature measurements were carried out with an in-house built horizontal translation type Curie balance with a sensitivity of ~5 × 10^{-9} Am^2 (Mullender et al., 1993). Anhysteretic remanent magnetization (ARM) was imparted in a 150 mT alternating field superimposed with a 40 μT direct bias field. Both types of remanent magnetization measurements were conducted at the paleomagnetic laboratory 'Fort Hoofddijk' of Utrecht University (Utrecht, The Netherlands).

To assess the relative content of the paramagnetic and ferromagnetic fraction of the samples, we analyzed the high-field and low-field slopes of the 'induced hysteretic' magnetization, defined by the mean value of the descending and ascending branch for a hysteresis loop (Fig. 2, Fabian and Von Dobeneck, 1997). The low-field slope, representing the overall contribution of the paramagnetic and ferromagnetic (sensu lato) fractions, is determined at a field of 0 T. The paramagnetic contribution is calculated by finding the slope of the linear high-field portion, with the field interval used for determining of the high-field slope varying based on the shape of the 'induced hysteretic magnetization' curve (the red dashed line in Fig. 2). A total of sixty hysteresis loops were analyzed in this study.

4. Results

Through the detailed comparison between magnetic fabrics and various rock magnetic behaviors (e.g., K_m, NRM, SIRM or ferromagnetic percentage), the twelve sites (comprising 120 specimens) are categorized into four distinct groups, labeled as Group I, II, III and IV. Group I includes sites 0, 1, and 7, exhibiting a site-mean K_m exceeding 1000 × 10^{-6} (SI). Groups II consists of sites 3, 4, 5, and 11, while Group III comprises sites 6, 8, 9, and 10. Groups II and III have K_m values between 500 and 1000 × 10^{-6} (SI) and between 200 and 500 × 10^{-6} (SI), respectively. The remaining site, site 2, has the lowest site-mean K_m of 208 × 10^{-6} (SI), but it displays distinct rock magnetic features, thus constituting Group IV by itself. Across Groups I to IV, there is a decrease in the values of T, NRM, SIRM, M_s and ferromagnetic percentage, while P_j shows an increase.

4.1. Rock magnetism

Previous rock magnetic studies have revealed that SP and stable SD authigenic magnetite are the dominant magnetic NRM carriers (see Fu et al., 2022 for more details, the site numbers here correspond to those in that study). The authigenic magnetite is formed as an oxidation product of iron sulfides. Groups I, II, and III show similar characteristics in routine rock magnetic experiments, including 'wasp-waisted' hysteresis loops, SP-dominated first-order-reversal-curve (FORC) diagrams, and IRM acquisition curves expressing a magnetically soft mineralogy (Fu et al., 2022). Group IV specimens show noisy IRM acquisition curves and interacting SD- or PSD/vortex-like FORC diagrams (Fu et al., 2022).

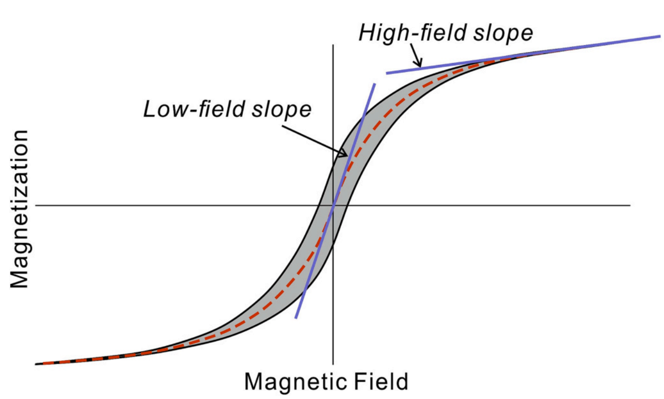

Fig. 2. A hysteresis loop of a sample consists of a descending branch and an ascending branch. The red dashed line is the 'induced hysteretic' magnetization, the average of the descending and ascending branches (terminology after Fabian and Von Dobeneck, 1997). The low-field slope is the slope at 0 T and high-field slope is the linear segment at high fields.

Stepwise high-field thermomagnetic runs of magnetization versus temperature were conducted for four specimens, each representing one of the four groups, to detect the alteration of iron sulfides during heating (Fig. 3). Generally, all specimens show (quasi)reversibility during heating/cooling below 350 °C. Irreversibility between heating and cooling cycles is observed at higher temperatures, starting at ~420 °C. An abrupt increase in magnetization occurs at ~410–420 °C during heating, likely indicating the alteration from pyrite to magnetite (Passier et al., 2001; Li and Zhang, 2005; Wang et al., 2008). The magnetic behaviors of pyrite during thermal treatment appear to be complicated. Pyrite can undergo alteration to pyrrhotite in an argon atmosphere at temperatures above 560 °C or in air above 600 °C, and to magnetite at lower temperatures (~350–500 °C; Li and Zhang, 2005). The newly formed magnetite can be reduced to monoclinic pyrrhotite by the unreacted pyrite (Wang et al., 2008). The minute discontinuity at 320 °C in the final cooling curve could well be attributed to the presence of pyrrhotite (Fig. 3A-C). The 'hump' present in the heating curve between 350 and 520 °C of the Group IV specimens may be due to the oxidation of pyrite and formation of magnetite (Li and Zhang, 2005; Wang et al., 2008; Fig. 3D).

Plotted on the Day diagram, ~40% of the data lie in the PSD field, displaying high values of M_{rs}/M_s and low values of B_{cr}/B_c. Specimens to the right of the PSD field exhibit low values of M_{rs}/M_s and high values of B_{cr}/B_c (Fig. 4A), accounting for ~60.0% of the data. Group I shows two distinct clusters: one within the upper PSD field and the other to the right of the PSD field (Fig. 4A). Many of the groups II-IV fall in the upper right corner of the PSD field and to its right (Fig. 4A). Although the Day plot for domain state diagnosis is somewhat ambiguous without additional constraints on the magnetic mineralogy and oxidation degree of the magnetite (Roberts et al., 2018), it remains a common method for providing a first-order overall presentation of the hysteresis parameters, especially in the case of remagnetized limestones. Here, we focus indeed on visualizing differences among the samples on the Day plot, rather than making firm statements pertaining to domain state. Furthermore, compared with common carbonates, NRM of the present limestones is rather strong (with an average value of ~10 mA/m), suggesting the in situ growth of a significant population of SP - stable SD particles (Katz et al., 2000; Font et al., 2006; Jackson and Swanson-Hysell, 2012). In line with this notion, the remagnetized limestones also exhibit higher NRM intensities than other samples in the Mirassol d'Oeste cape, Brazil (~1 mA/m) (Font et al., 2006). The NRM decreases from Group I to Group IV, and Group I has an average NRM about one order of magnitude greater than that of Group IV (Fig. 4B). In addition, the paramagnetic and ferromagnetic fractions were evaluated. Ferromagnetic minerals contribute >90% to the total magnetization in Group I, while this contribution ranges 80–90% in groups II-IV. Group III is variable, with specimens exhibiting notably high or low ferromagnetic contribution; the ferromagnetic fraction in this group is slightly lower than in groups II and IV (Fig. 4C). The positive correlation between NRM and the ferromagnetic phase percentage reveals the variable concentration of SP - stable SD magnetite in these groups (Fig. S2).

4.2. Anisotropy of magnetic susceptibility

One hundred and twenty specimens from twelve sites were processed. The sampled section is monoclinal: the bedding attitudes change slightly with a dip direction of ENE and dips of ~20–30° (Fig. 1D). Overall, stereonet projections show that the K_1 and K_3 AMS ellipsoid axes are generally well grouped (Fig. 5A, B). K_1 exhibits a nearly horizontal orientation, with an average inclination of 16.2° (standard deviation, σ = 17.8°), while K_3 shows a rather steep inclination, with an average inclination of 50.3° (σ = 26.4°) in stratigraphic coordinates. In addition, K_1 shows a dominant NE-SW distribution, while K_3 and K_2 form a girdle-like distribution in the NW-SE vertical plane (Fig. 5B). The specimens show an average low-field susceptibility of 624 × 10^{-6} (SI) (σ = 380× 10^{-6} (SI)) ranging from 31 × 10^{-6} to 1527 × 10^{-6} (SI) (Fig. 5C,

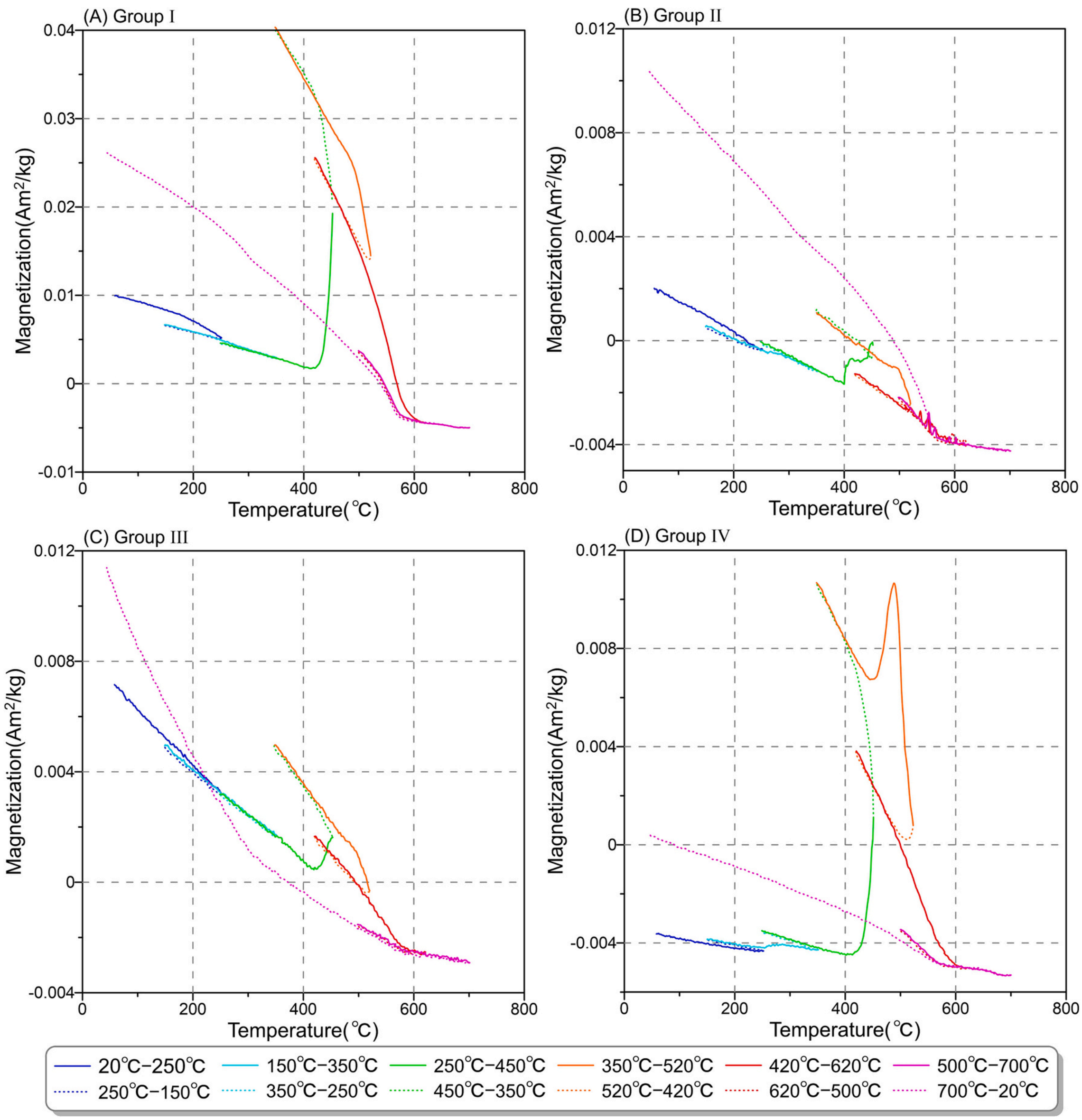

Fig. 3. High-field thermomagnetic runs of representative specimens of each group. Solid (dashed) lines indicate the heating (cooling) curves.

Supplementary material Table S1). The corrected anisotropy degree (P_j) ranges from 1.007 to 1.095, with an average ± standard deviation of 1.039 ± 0.018 (Fig. 5D). A poor linear correlation between K_m and P_j suggests that the P_j is independent of the magnetic mineral concentration (Li et al., 2020a, 2021; Fig. 5D). The shape parameter T is variable, with an average value of −0.281 and a range between −0.922 and 0.878 (Fig. 5E), indicating a balanced distribution of samples with oblate and prolate ellipsoids. The magnetic foliation (F) exhibits a relatively narrow distribution ranging from 1.001 to 1.057 ($F_{mean} = 1.018$, $\sigma = 0.018$), similar to the magnetic lineation (L) that ranges from 1.002 to 1.054, with an average value of 1.019, $\sigma = 0.017$. The F-L plot (Flinn diagram) shows the same oblate/prolate character of distributions (Fig. 5F). On the box and whisker plots, a negligible increase in P_j and a decrease in T are noticeable when going from Group I to Group IV, albeit that the within-group spreading is rather large (Fig. 6C,D). The interquartile ranges of the box and whisker plot are large, so this trend is deemed statistically insignificant.

While the magnetic lineation ($L = K_1/K_2$, parallel to K_1) is consistently horizontal and oriented NE-SW (with minor variations), the K_3 orientations tend to be more dispersed, distributed in a plane perpendicular to the lineation. Group I specimens have the highest average susceptibility of ~1200 × 10^{-6} (SI) and the lowest paramagnetic mineral percentage (Fig. 6A, B, Table 1). The K_1 of Group I is well clustered, showing a horizontal arrangement with a NE-SW direction (~40°), while the K_3 axis shows a NW-SE distribution (~144°) (Fig. 7A). It is noteworthy that K_3 orientations may be treated as two rather tight clusters: one characterized by a steep, almost vertical inclination, and the other with an intermediate inclination and SE direction. Alternatively, the entire distribution could be construed as a girdle along the vertical SE-NW plane. Given the consistent characteristics in K_m, P_j, T, and ferromagnetic percentage within this group, the second proposition is preferable, that is, considering K_3 as a girdle. Group II specimens have a lower average susceptibility of ~700 × 10^{-6} (SI) and a contribution of ferromagnetic minerals of ~90% (Fig. 6A, B). The majority of K_1 orientations in these specimens follow a NE-SW distribution, while some specimens are oriented in the NW-SE direction (Fig. 7B). The overall direction defined by the K_1 axis (~40°) is virtually identical to that of the Group I specimens (Fig. 7A, B, Table 1). Furthermore, K_3 orientations in the majority of specimens shows a rather shallow inclination along the SE direction. Group III and Group IV specimens display similar AMS distributions but differ in rock properties (Figs. 4, 7C, D). The K_1 and K_2 axes are grouped roughly in the bedding plane, and thus the K_3

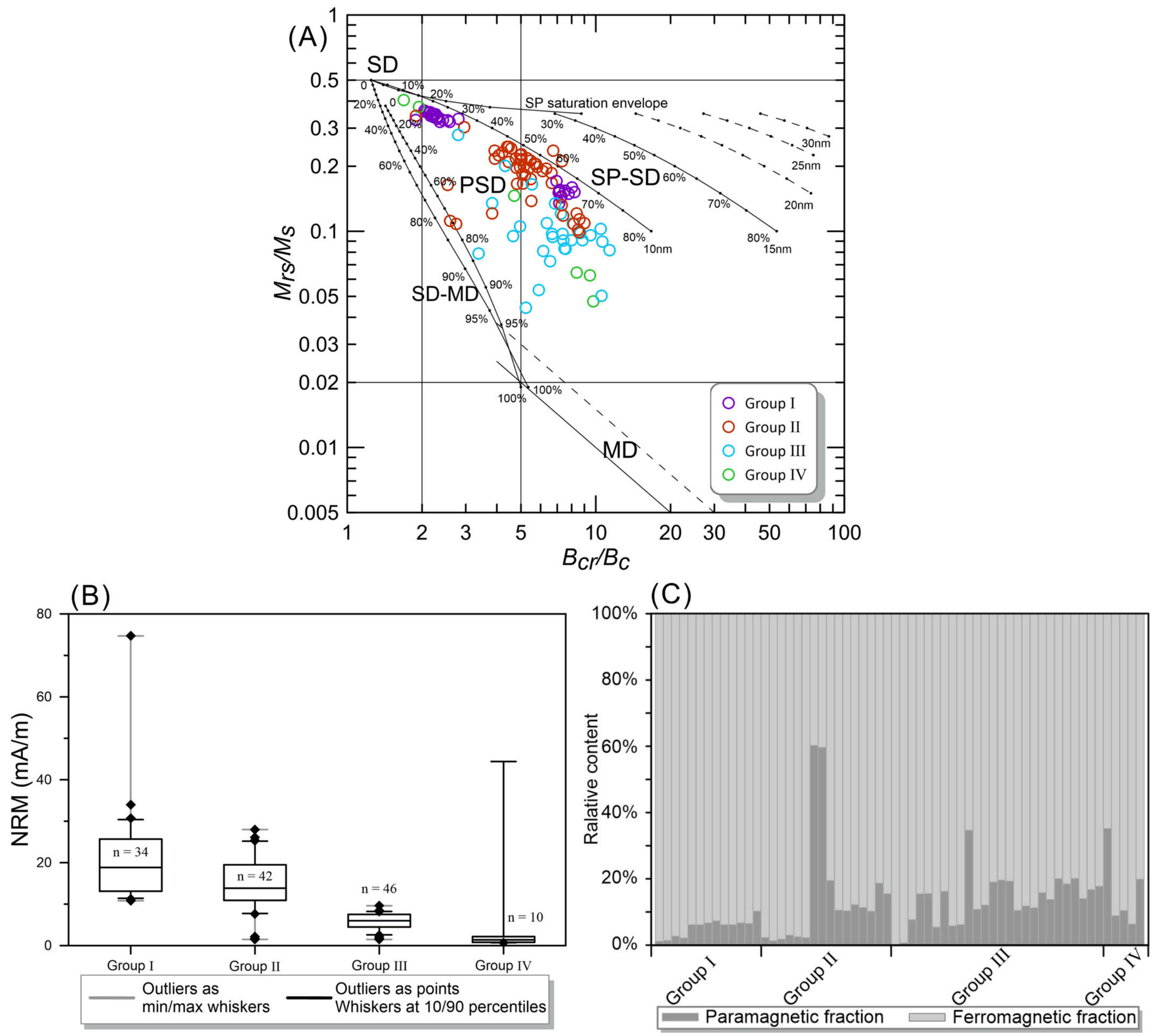

Fig. 4. (A) Day plot of representative samples from the four groups (after Dunlop, 2002). (B) Box and whisker plots of the starting NRM values of each group also showing the outliers. (C) Paramagnetic and ferromagnetic fractions for representative samples of each group (12, 16, 26 and 5 hysteresis loops were analyzed in Group I, II, III and IV, respectively).

axis is clustered around the bedding pole. The directions of these two groups, as defined by K_1, differ by ~20°: the K_1 axis of Group III has a declination of ~50°, while that of Group IV has a declination of ~30° (Fig. 7C, D, Table 1). However, it is important to note that the difference could be due to the rather limited number of specimens in Group IV, as some overlap between K_1 and K_3 orientations in these two groups is observed (Fig. 7C, D). In addition, Group IV specimens have the lowest average susceptibility of $\sim 100 \times 10^{-6}$ (SI) and a ferromagnetic mineral percentage of ~90% (Fig. 6A, B).

5. Discussion

5.1. Carriers of magnetic susceptibility

The total magnetic susceptibility of a rock is the sum of the contributions from all minerals present, including diamagnetic (most of the primary rock-forming minerals such as quartz, calcite, and feldspars), paramagnetic (many important auxiliary minerals such as hornblende, biotite, and clay minerals), antiferromagnetic (hematite, goethite), and ferrimagnetic (sensu stricto) minerals (e.g., magnetite, greigite, and pyrrhotite) (Jackson, 1991; Butler, 1992). The bulk susceptibility is influenced by the relative abundances and specific susceptibilities of these minerals. On the other hand, minerals with diverse origins may respond differently to deformation processes. Thus, identifying the mineralogical sources of AMS is of great significance in deciphering these susceptibilities (Rochette, 1987b; Rochette et al., 1992; Borradaile, 1988; Jackson, 1991; Borradaile and Jackson, 2010; García-Lasanta et al., 2018; Calvín Ballester et al., 2018a).

Early investigations mostly focused on the ferromagnetic (sensu lato) minerals, considering them as the major carriers of AMS (Hargraves and Fischer, 1959; Fuller, 1963, 1969). However, later studies suggested that paramagnetic minerals might significantly contribute to AMS in sedimentary rocks, given their often more substantial volume fraction compared to ferromagnetic minerals in rocks (e.g., Hounslow, 1985;

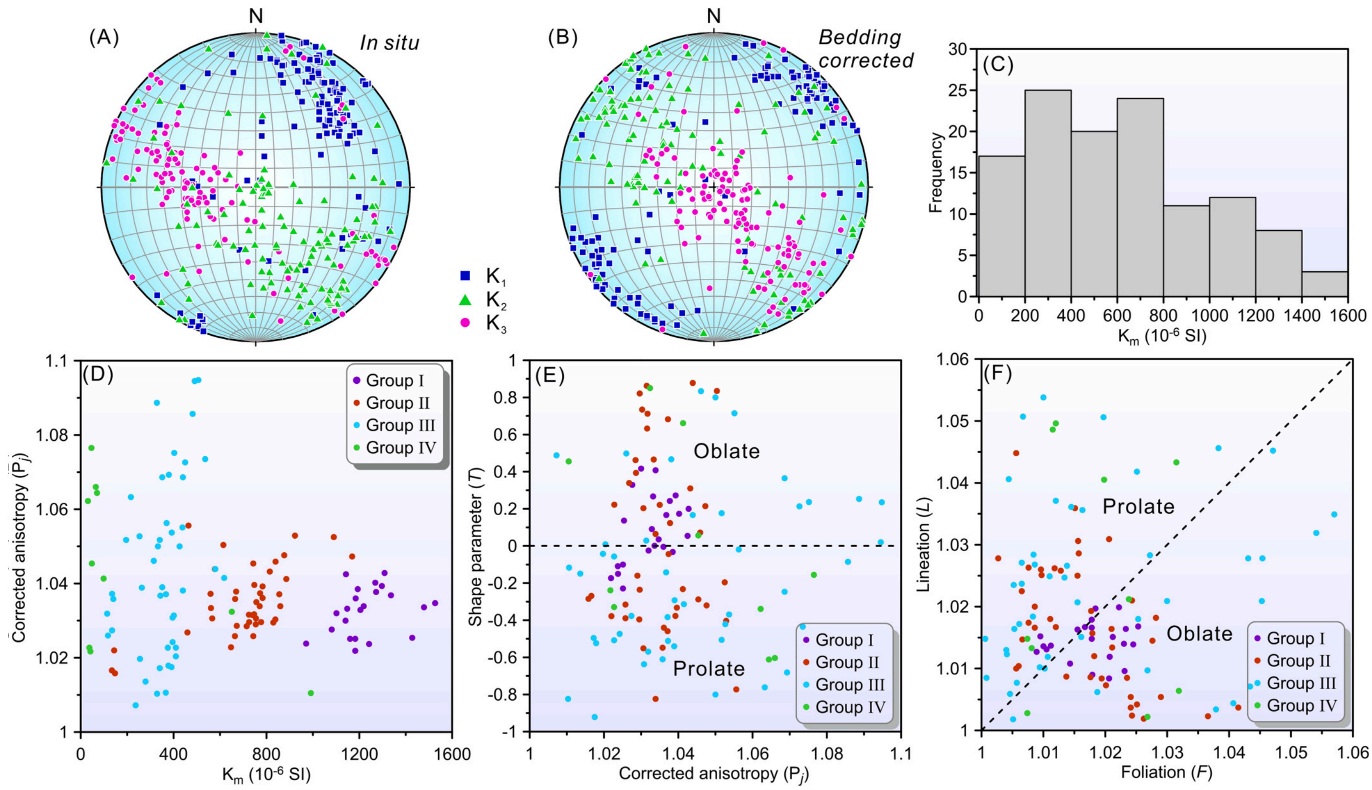

Fig. 5. Low field anisotropy of magnetic susceptibility results for the Jurassic limestones. In situ (A) and bedding-corrected (B) equal-area stereographic projections of the AMS principal axes (squares, triangles and circles show orientations of K_1, K_2 and K_3 axes, respectively). (C) Histogram of the mean magnetic susceptibility (K_m) ($N = 120$ specimens). (D) Mean magnetic susceptibility (K_m) versus corrected anisotropy degree (P_j) plot. (E) P_j versus shape parameter (T) plot. (F) Foliation F (K_2/K_3) versus lineation L (K_1/K_2) plot (Flinn diagram (Flinn, 1965)).

Rochette, 1987b; Rochette et al., 1992; Lüneburg et al., 1999; Parés, 2004; Cifelli et al., 2004, 2005, 2009; Li et al., 2020a, 2020c, 2021; Cao et al., 2021). Our previous investigation has revealed that authigenic magnetite grains, dominantly in the stable SD and SP size range, are responsible for the secondary magnetizations in the studied Jurassic limestones in the Zaduo area (Fu et al., 2022). It is important to note that the carriers of the magnetic remanence are not necessarily the same as those of the AMS. For example, sedimentary rocks deposited during the Late Paleozoic Ice Age in the Paraná Basin of South America were remagnetized during the Cretaceous, while their AMS was not overprinted by the secondary magnetic overprints, as AMS is carried by paramagnetic minerals (Bilardello, 2021).

Many studies follow a common criterion to estimate the contributions of ferromagnetic and paramagnetic minerals, where susceptibilities exceeding 5000×10^{-6} (SI) suggest dominance by ferromagnetic minerals, susceptibilities below 500×10^{-6} (SI) indicate control by paramagnetic minerals, and susceptibilities between 500 and 5000×10^{-6} (SI) imply mixtures of ferromagnetic and paramagnetic fractions (Rochette, 1987a, 1987b; Borradaile, 1987; Hrouda and Jelinek, 1990; Tarling and Hrouda, 1993). However, this criterion is equivocal, and more comprehensive investigations are required to reduce the ambiguity (García-Lasanta et al., 2015; Wang et al., 2017). In the present study, microscopic observations have shown that the diamagnetic rock-forming minerals calcite and quartz account for 98% of the rock in most samples (Fu et al., 2022). Keep in mind that calcite is quickly paramagnetic when Fe and/or Mn substitution is present, and so is quartz when it has a coating of ferrous/ferric iron ((oxy)hydr)oxides. The magnetic susceptibility values of all specimens range from 31×10^{-6} to 1527×10^{-6} (SI), with a median of 572×10^{-6} (SI) and an average of 624×10^{-6} (SI). Previous studies have indicated that remagnetized limestones typically have higher susceptibility than non-remagnetized limestones (Katz et al., 2000; Font et al., 2006; Jackson and Swanson-Hysell, 2012). Given that magnetite has susceptibility approximately six orders of magnitude larger than that of calcite (Jackson, 1991), a plausible interpretation for the observed difference is that our limestone samples contain a relatively high but variable concentration of authigenic magnetite grains.

Magnetic remanence exclusively resides in ferromagnetic (sensu lato) minerals. To qualitatively verify whether susceptibility and remanence (the natural characteristic remanent magnetization, and/or the ARM or IRM induced in the laboratory) reside in the same mineral, their comparison has been shown to be insightful (Lowrie and Heller, 1982). Overall, our specimens exhibit positive correlations between susceptibility and various remanences or saturation magnetization (i.e., K_m versus NRM, K_m versus SIRM, and K_m versus M_s) (Fig. 8 and S1; Supplementary material Table S1). Group I appears to be more scattered than the other three groups on all plots, revealing two distinct subgroups in the plot of K_m versus SIRM (Fig. 8B). It is conceivable that the scatter of this group may result in bias to the correlations. Better correlations are present on plots of K_m versus SIRM and K_m versus M_s than that of K_m versus NRM. This discrepancy could be attributed to the fact that NRM typically is composed of multiple remanence components acquired at different times during the rock's geological history (Tauxe, 2010). In contrast, isothermal magnetization parameters are faithfully acquired in the laboratory, providing a more comprehensive insight into rock magnetic analysis (e.g., Fabian and Von Dobeneck, 1997; Aben et al., 2014). The correlations between susceptibility and NRM, as well as various laboratory rock magnetic properties, indicate a common mineral carrier for susceptibility and remanence, that is, authigenic magnetite in our study (Fu et al., 2022).

5.2. Diagnosis of the inverse magnetic fabric

A normal magnetic fabric is described as a type of anisotropy with

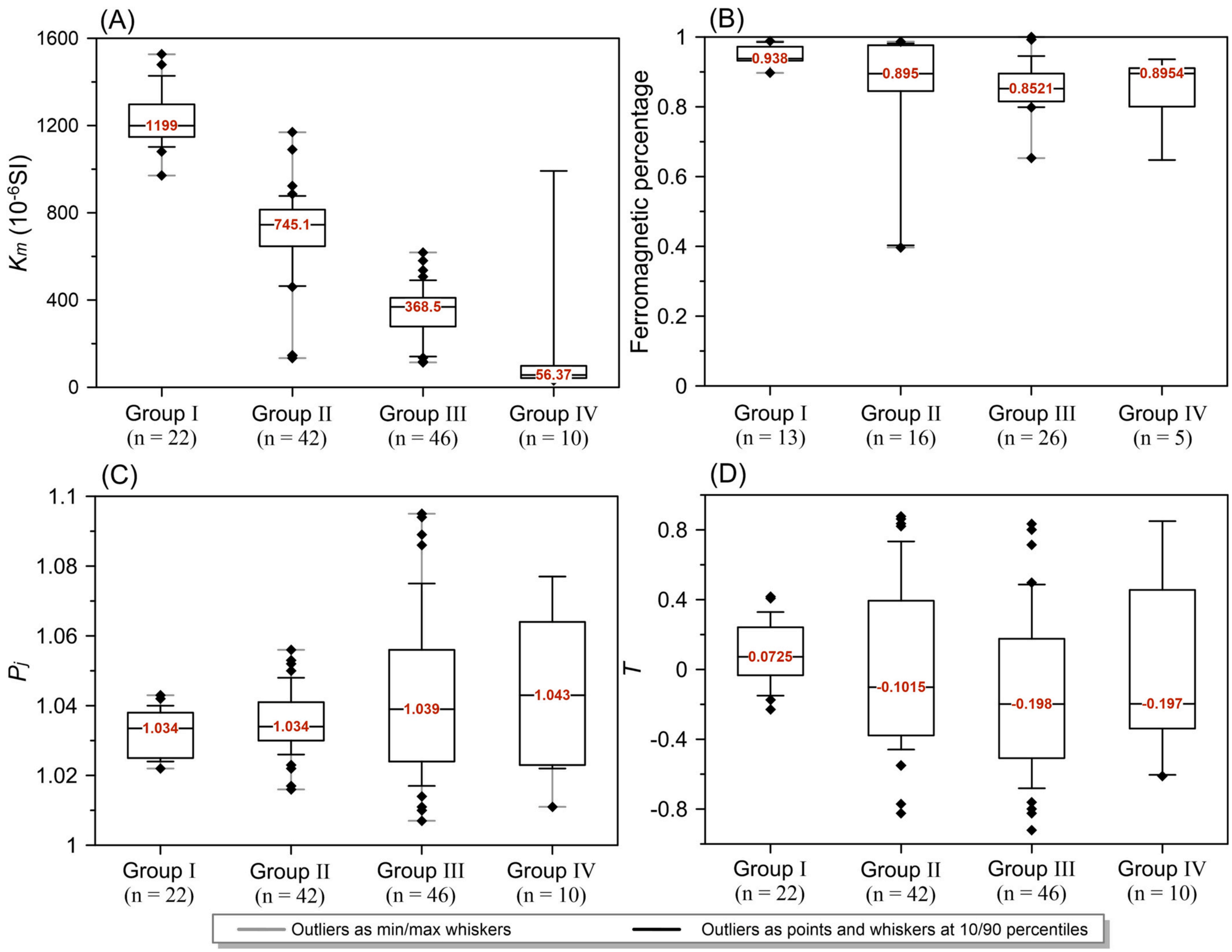

Fig. 6. Box and whisker plots showing the median (horizontal lines in the boxes) and the quartiles of the different parameters measured in the specimens. (A) Bulk susceptibility (K_m) at room temperature. (B) Ferromagnetic contribution (% Ferro) to the total bulk magnetic susceptibility expressed as a percentage. (C) Corrected degree of anisotropy (P_j) of the AMS. (D) Shape parameter (T) of the AMS.

the K_1 axis parallel to the long axis of the crystal (the easy direction of magnetization). Occasionally, an inverse magnetic fabric occurs when the K_1 axis is perpendicular to the long axis of the crystal (Fig. 9; Rochette, 1988; Potter and Stephenson, 1988). In the case of SD magnetite, a magnetic field (H) applied perpendicular to the long axis of magnetite particles causes the rotation of particle magnetization (M) toward the field direction to minimize the total energy, resulting in a susceptibility with $dM/dH > 0$. Conversely, when the field is imparted parallel to the long axis, there is no angular gradient in the energy balance to rotate the magnetization, leading to $dM/dH = 0$ (Jackson, 1991). This phenomenon is referred to as the ‘SD effect’ in magnetite.

The comparison between bulk susceptibility and various natural and laboratory rock magnetic properties reveals that the susceptibility and remanences are governed by the same magnetic carriers. This observation forms the basis for quantifying grain size using the ratio of susceptibility (mass-specific χ) to field-normalized ARM (χ_{ARM}). Previous studies have shown that the χ/χ_{ARM} ratio typically reaches its minimum value within the grain size range corresponding to SD particles, and MD grains exhibit a higher χ/χ_{ARM} ratio compared to PSD grains (Dankers, 1978; Özdemir and Banerjee, 1982; Maher, 1988). Specimens from groups I through III exhibit a χ/χ_{ARM} ratio lower than 200, with a significant proportion of values even below 100, while Group IV specimens show higher values (Fig. 10). A χ/χ_{ARM} ratio of 100 corresponds to an experimentally estimated grain size range of 20 nm to 90 nm (Maher, 1988; Liu et al., 2004; Fig. 10). The calculated average ratio from our specimens is 108, implying that SD magnetite grains dominate the magnetic carriers. The ‘SD effect’ in the magnetite is the rationale for the inference of an inverse magnetic fabric.

Large quantities of uniaxial SD (USD) magnetite have been identified in remagnetized carbonates (e.g., Jackson and Swanson-Hysell, 2012; Calvín Ballester et al., 2018b). Plotted on a Day plot, our data plots along the SD + SP trend (Fig. 4A), as expected for remagnetized limestones (e.g., Channell and McCabe, 1994). On a Néel diagram (Néel, 1955; Tauxe et al., 2002), our data plots to the left of the line from the origin to USD particles with an axial ratio of 1.3:1 (Fig. 11). The authigenic magnetite grains grew evenly, resulting in small axial ratios. Since shape and grain size are major controlling factors for magnetite anisotropy, even slight deviations from equant grains induce uniaxial magnetic anisotropy (e.g., Winklhofer et al., 1997; Evans et al., 2003; García-Lasanta et al., 2018). Indeed, the data plot falls between the cubic SD + SP trend line and uniaxial SD + SP field (Fig. 11). Thus, the authigenic magnetite in the remagnetized limestones would give rise to an inverse magnetic fabric.

It appears that the susceptibility correlates with the ferromagnetic percentage of the specimens (Fig. 6A, B). The decreasing trend in K_m from Group I to IV aligns with the decline in the ferromagnetic percentage from Group I to III, while Group IV is somewhat inconsistent

Table 1
Scalar parameters of the AMS for the remagnetized limestones.

Site	n	K_m	L	F	P_j	T	K_1		K_2		K_3	
		(10^{-6}) SI					Dec	Inc	Dec	Inc	Dec	Inc
Group I												
Site 00	6	1269	1.017	1.016	1.033	−0.03	57.1	8.4	147.7	3.8	261.7	80.7
Site 01	6	1269	1.017	1.016	1.033	−0.03	49.3	14	147.2	29	296.6	57.2
Site 07	11	1223	1.013	1.02	1.034	0.211	31.7	15.7	281	51.5	132.7	34.1
Mean	23	1231	1.018	1.007	1.026	−0.45	40.5	10.5	302.8	36.1	144.2	51.9
Group II												
Site 03	10	713	1.011	1.014	1.024	0.135	329.5	15	63.2	13.5	193.5	69.6
Site 04	11	846	1.007	1.011	1.018	0.185	37.6	5.9	292.1	68.8	129.8	20.3
Site 05	9	736	1.023	1.007	1.031	−0.56	217.8	5.6	313	42.6	121.7	46.9
Site 11	12	542	1.005	1.022	1.028	0.654	230.3	5	340.6	75.9	139.2	13.2
Mean	42	704	1.009	1.009	1.018	−0.03	39.6	4.4	303.6	53.9	132.7	35.7
Group III												
Site 06	12	443	1.028	1.038	1.067	0.145	36.3	3.6	305.1	18	137.2	71.6
Site 08	11	251	1.023	1.011	1.034	−0.36	230.6	8.6	322	9.2	98.2	77.4
Site 09	12	328	1.017	1.007	1.024	−0.43	58.2	2.4	328	3.6	181.5	85.7
Site 10	11	382	1.017	1.002	1.021	−0.76	245.7	8.1	340.1	28.5	141.4	60.2
Mean	46	352	1.019	1.015	1.035	−0.13	230.1	1.9	320.6	15.7	133.2	74.2
Group IV												
Site 02	10	208	1.02	1.017	1.037	−0.1	33.7	1.9	123.7	1.6	253.5	87.6

Notes: n: number of specimens used to calculate the AMS; K_m: mean magnetic susceptibility for all specimens of each site/group; *L*: magnetic lineation; *F*: magnetic foliation; P_j: corrected anisotropy degree; *T*: shape parameter; Dec, Inc.: declination (azimuth) and inclination (plunge), respectively, of the K_1, K_2, and K_3 axes after bedding correction.

possibly due to its small size. In contrast, there is a significant decline in K_m and a subtle ascending in P_j, suggesting an inverse relationship with the anisotropy degree (Fig. 6A, C). This trend is also observable in the K_m - P_j diagram (Fig. 5D). The negative correlation between susceptibility and P_j can be attributed to counteracting anisotropy ellipsoids of stable SD and SP magnetic grains. SP magnetite has a higher susceptibility than stable SD magnetite. The decrease in K_m values observed from Group I to IV is associated with a diminishing relative contribution of SP magnetite across these groups (note also their NRM is declining along similar lines). On the other hand, stable SD magnetite typically exhibits an inverse magnetic fabric, while SP magnetite displays a normal magnetic fabric. The mixing of these two magnetic fabrics results in intermediate fabrics (Ferré, 2002; Calvín Ballester et al., 2018a). In scenarios where stable SD particles are still dominant over SP particles, a higher amount of SP magnetite lowers the anisotropy (Calvín Ballester et al., 2018a), i.e., the overall anisotropy diminishes, while the orientation of its principal axes remains unaltered.

Alternatively, from a geological setting point of view, the collision between India and Eurasia led to N-S shortening, which is obviously different from the direction perpendicular to the K_1 measured in the present study. The declination of the site-mean direction in stratigraphic coordinates (Ds) is 30.6° ± 3.2° (Fu et al., 2022). Given the rotation of the Zaduo area after the India-Eurasia collision, the compression direction is more likely represented by the magnetic lineation, that is, the inverse magnetic fabric present.

5.3. Authigenic magnetite under deformation and its tectonic implications

The oxidation of iron sulfides, here primarily pyrite, to authigenic magnetite is interpreted as the remagnetization mechanism in the studied carbonates (Fu et al., 2022). It is conceivable that the authigenic magnetite could produce a new fabric recorded during the remagnetization, as the oxidation of iron sulfides to authigenic magnetite is not a topotactic reaction (Calvín Ballester et al., 2018a). Studies into AMS of remagnetized carbonates with SD magnetite as the magnetic carrier have revealed a synchronous acquisition of secondary remanence and the associated AMS (Sun et al., 1993; Calvín Ballester et al., 2018a). Small magnetite particles at the nanoscale residing in the pyrite grains (or in cracks or at the surface) grew as rims in remagnetized rocks (e.g., Suk et al., 1993; Blumstein et al., 2004; Oliva-Urcia et al., 2009; Kars et al., 2014; Calvín Ballester et al., 2018a; Calvín Ballester et al., 2018b). Pyrite grains prevent magnetite inclusions from being affected by the external deformation regime. Thus, magnetite grains can form under infinitesimal strain (equivalent to the stress conditions), i.e., independent of previous sedimentary or tectonic structures (Sun et al., 1993; Calvín Ballester et al., 2018a; Calvín Ballester et al., 2018b). Following this rationale, the alteration of precursor sulfides to authigenic magnetite during remagnetization is conditioned by contemporary dynamic factors, such as the prevailing compression field (Calvín Ballester et al., 2018a, Calvín Ballester et al., 2018b).

The India-Eurasia collision and the subsequent uplift of the Tibetan Plateau belong to the most significant geological events in the Cenozoic (Yin and Harrison, 2000; Ding et al., 2017). This collision caused a 20° ± 3.0° clockwise rotation of the Zaduo area relative to Eurasia since the Paleogene (Fu et al., 2022). Passive rotation of the magnetic fabric occurred during the rotation of host block (e.g., Larrasoaña et al., 2004; Weil and Yonkee, 2009; Wang et al., 2017). The group-mean directions of the K_1 axis range from ~33° to 50° and yield an overall average of 43.1° ± 6.9° (Fig. 7; Table 1). The variability in the K_1 axis directions is likely associated with magnetite growth during rotation, or measurement uncertainties and local structural 'noise'. If the magnetite was grown during rotation, one would anticipate a discernible relationship between the paleomagnetic orientation and the declination of K_1. However, the correlation between these two parameters is relatively weak (Fig. 12), making magnetite growth during rotation less probable. The well-clustered paleopoles of the sites (Fu et al., 2022) imply a coherent pattern of rotation. Thus, the paleo-compression orientation can be restored by undoing the rotation of the Zaduo area.

The restored paleo-compression direction ranges from ~13° to 30°, with an average of 23.1° ± 6.2°. This orientation notably differs from the present-day ENE-WSW shortening direction of ~70°, as obtained from GPS data (Wang and Shen, 2020). In more detail, the restored K_1 axis direction of Group IV displays nearly N-S compression (~13°), groups I and II show a ~20° compression direction, and Group III

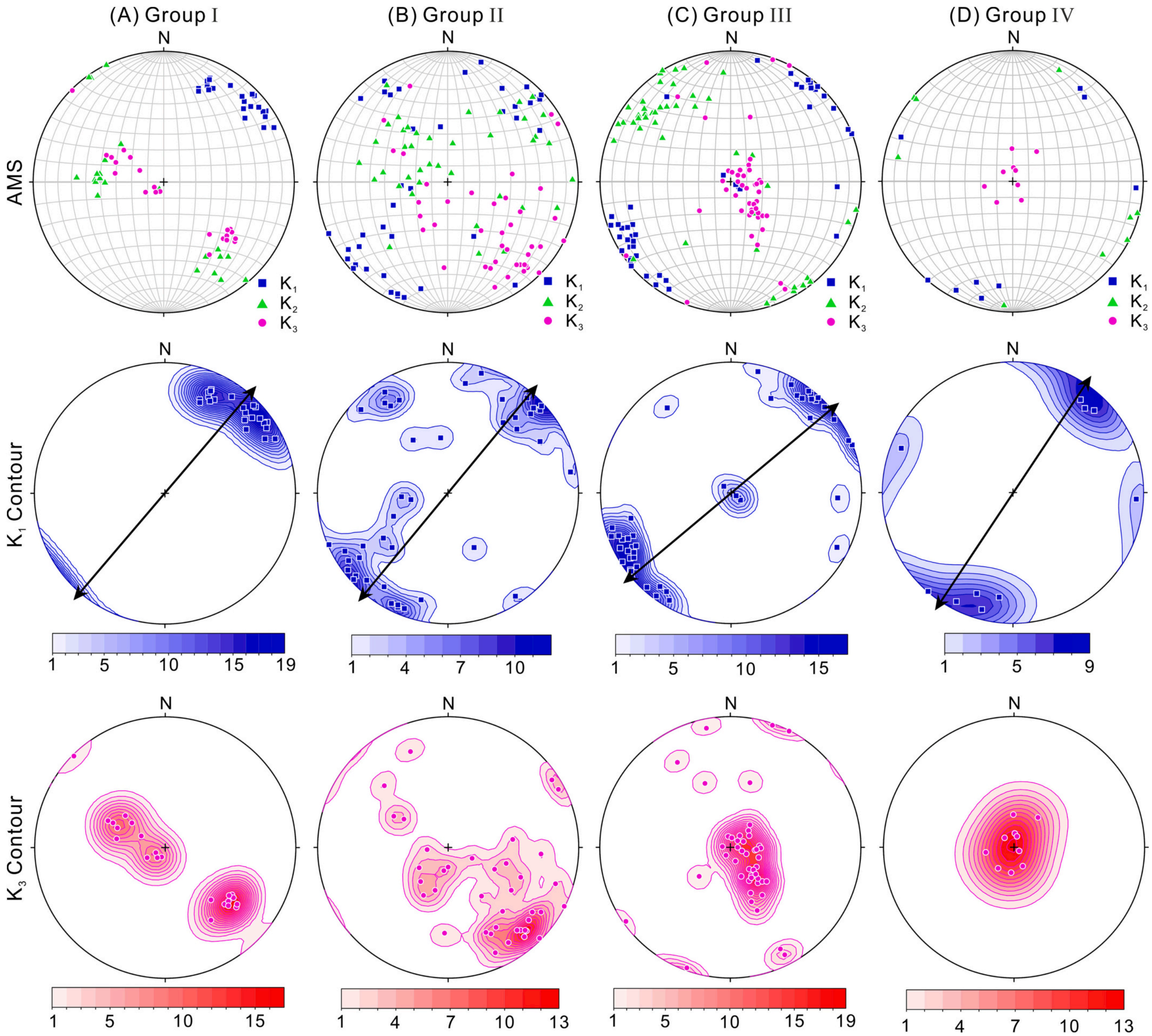

Fig. 7. Stereographic lower-hemisphere projections of the magnetic susceptibility axes after bedding-correction. The contours of variable colors represent the distribution of percentage densities of the K_1 (blue) and K_3 (red) axes. Black arrows (K_1) represent the trend of the mean magnetic lineation. (For interpretation of the references to colour in this figure legend, the reader is referred to the web version of this article.)

indicates a NNE-SSW compression direction of ~30°. It is worth noting that several specimens from site 3 of Group II show a NW declination of K_1, which could be interpreted as indicative of a normal magnetic fabric.

Research conducted in the Gongjue Basin, a Cenozoic basin situated southeast of the Zaduo area, presents slightly different compressional regime. Li et al. (2020c) present AMS data from sediments with an age ranging between ~69 Ma and 41 Ma in the central Gongjue Basin, while Xiao et al. (2021) suggest an age for the basin between ~69 Ma and 50 Ma. Despite disagreement on the age model in these studies, the overall orientation of the K_1 axis in their AMS data is tightly clustered along the NNW-SSE direction. The magnetic susceptibility is mainly carried by hematite, paramagnetic minerals and some magnetite, indicating a normal magnetic fabric. Their results reveal ENE-WSW tectonic compression perpendicular to the K_1 axis (Li et al., 2020c; Xiao et al., 2021). A robust correlation between paleomagnetic declinations and K_1 declinations in AMS (Li et al., 2020c) indicates that the AMS orientation is controlled by the rotation of the Gongjue area. The magnetostratigraphic results from Li et al. (2020c) propose a ~30°-40° clockwise rotation of the Gongjue area relative to Eurasia. The paleo-compression direction of the Gongjue area can be restored to ~35° to 45°, with an average of ~40° (Fig. 13B).

The structural trend in the Zaduo and Gongjue areas can be quantified by averaging their respective regional fault strikes. In the Zaduo area, 166 faults yield a structural trend of ~125°, while in the Gongjue area, 79 faults produce a trend of ~145° (Qinghai Geological Survey Institute (QGSI), 2005; Xizang Geological Survey, 2007; Fig. 13A). Thus, the difference in structural trend between the two regions is ~20°, in line with their difference in rotation (~10°-20°). However, the compression directions differ by ~30°-40°, i.e., slightly larger than the differences in rotation. After the restoration of the later rotation, an Eocene NNE-SSW compression is obtained in the Zaduo area, and a NE-SW compression in the Gongjue area (Fig. 13B). In the Mangkang area, more to the East than the Gongjue area, a total of 135 faults yield a trend of ~158° (Qinghai Geological Survey Institute (QGSI), 2005; Xizang

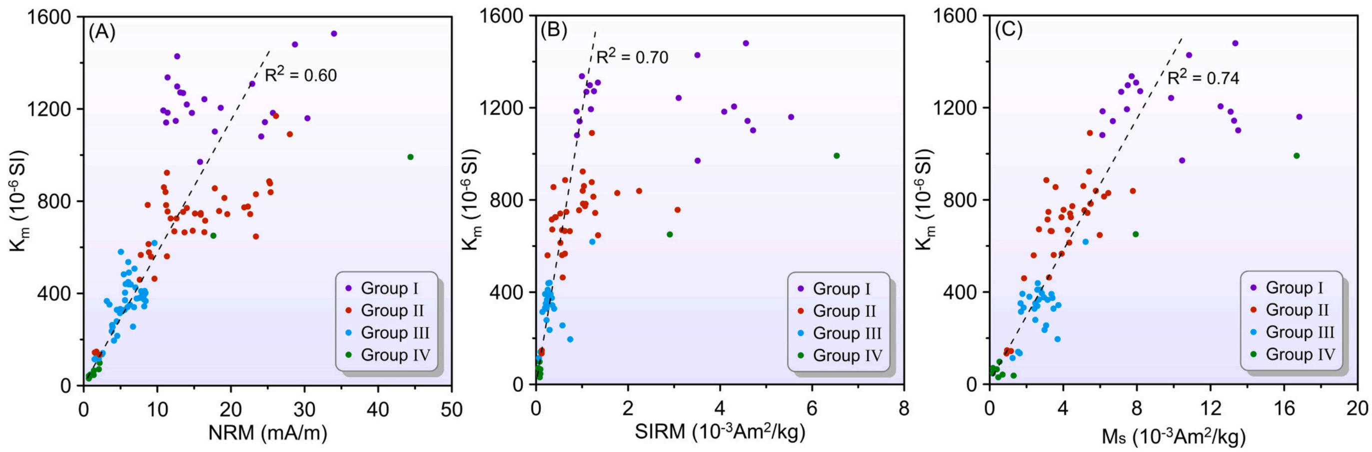

Fig. 8. Remagnetized limestones: Correlation between (A) mean magnetic susceptibility (K_m) and natural remanent magnetization (NRM); (B) K_m and saturation isothermal remanent magnetization (SIRM); (C) K_m and saturation magnetization (M_s).

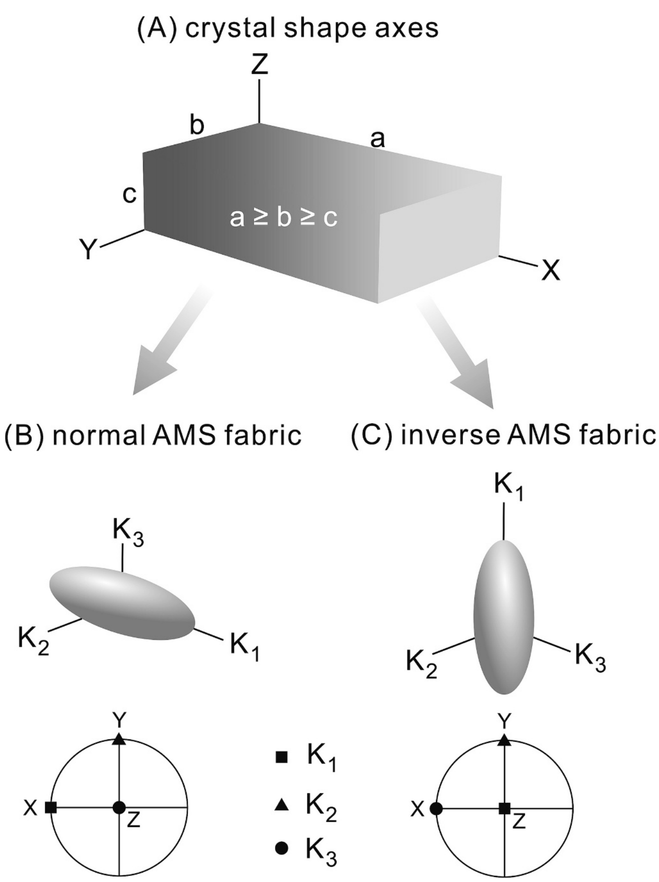

Fig. 9. Relationship between crystal shape axes and principal axes of magnetic susceptibility, modified from Ferré (2002). (A) Crystal shape axes. (B) Normal magnetic fabric. (C) Inverse magnetic fabric. The upper figure in (B) and (C) represents the magnetic susceptibility ellipsoid, and the lower figure in (B) and (C) shows the orientation of the magnetic susceptibility axes (X, Y, and Z refer to the orientation of the crystal shape axes).

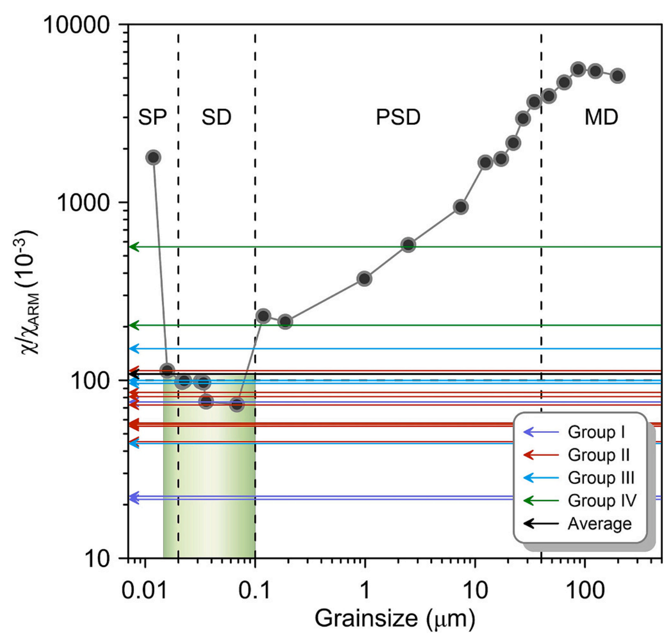

Fig. 10. Plot of χ/χ_{ARM} versus grain size for synthetic magnetite, modified from Liu et al. (2004). Black dots mark the χ/χ_{ARM} ratio summarized by Liu et al. (2004) from Dankers (1978) (d > 1 μm), Özdemir and Banerjee (1982) (70 nm < d < 11 μm), and Maher (1988) (d < 70 nm). Vertical dashed lines mark the grain size of the domain state boundaries, while the horizontal dashed line corresponds to the grain size ranging from 20 to 90 nm. Horizontal solid lines of various colors indicate the χ/χ_{ARM} values determined in this study, and the green shading marks the estimated grain size in this study. (For interpretation of the references to colour in this figure legend, the reader is referred to the web version of this article.)

Geological Survey, 2007; Fig. 13A). Furthermore, a paleomagnetic study reveals a larger clockwise rotation since the Cretaceous in this area (Tong et al., 2015). These results hint at a secondary orocline around the EHS, formed during the India-Eurasia collision. Taken our AMS data and the published data in the Gongjue area, we suggest that the India-Eurasia convergence might have occurred in a NNE-SSW to NE-SW direction, in line with the trajectory of the Indian plate relative to fixed Eurasia (van Hinsbergen et al., 2011; Todrani et al., 2022). The deceleration of the convergence implies a stronger resistance of Eurasia (Pusok and Stegman, 2020; van Hinsbergen et al., 2011), likely resulting in regionally different compression directions (Fig. 13B). AMS proves to be a sensitive strain indicator, capable of recording a strain direction even when the strain has resulted in no/very limited regional rotation (Luo et al., 2013). In the north of the EHS, at least in the Qamdo region (Gongjue and Mangkang areas) and the Zaduo area, it is the northward compression rather than rotation that dominated the far-field effect of the India-Eurasia collision before the late Eocene. Subsequently, widespread clockwise rotation of the southeast Tibetan Plateau occurred

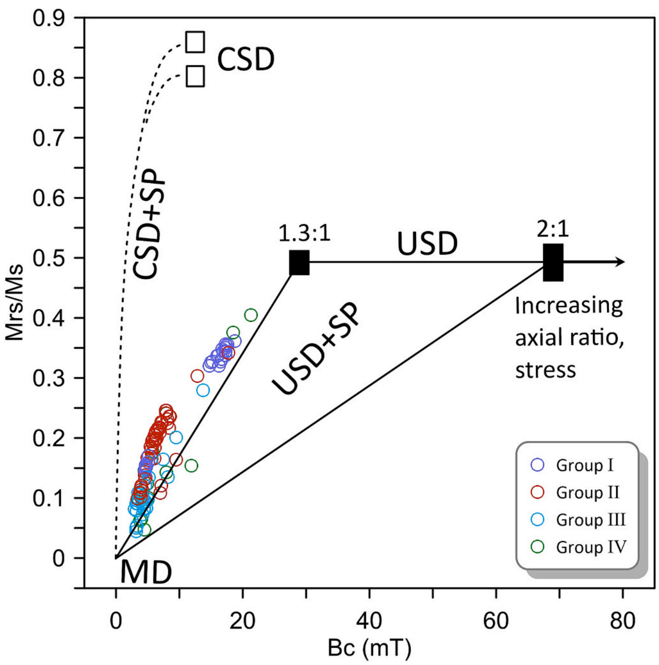

Fig. 11. Néel diagram (Néel, 1955) of representative samples from the four groups, with a slightly modified interpretive framework provided by Tauxe et al. (2002); USD = uniaxial single domain; CSD = cubic single domain.

after the late Eocene (e.g., Tong et al., 2017, 2022; Zhang et al., 2020; Li et al., 2020b, 2020c; Todrani et al., 2022; Fig. 13C).

In summary, we have identified an inverse magnetic fabric in the Jurassic Buqu Formation limestones that underwent remagnetization in the Eocene. The growth of authigenic magnetite generated both the secondary NRM and the associated AMS. Together with the AMS data from the Gongjue area, the inverse magnetic fabric of our study provides a picture of how the orocline developed around the EHS. The Eocene compression, with a NNE-SSW orientation in the Zaduo area and a NE-SW orientation in the Gongjue area, represents an early response to the India-Eurasia collision. The variations in compression led to larger clockwise rotations in the Gongjue area compared to the Zaduo area surrounding the EHS.

6. Conclusion

This study focused on the magnetic fabrics of limestone outcrops in the Zaduo area, EQT, examining twelve sites comprising a total of 120 specimens. The Jurassic rocks under investigation are reported to have been chemically remagnetized during the Cenozoic, giving rise to stable SD and SP authigenic magnetite. Overall, the determined average low-field susceptibility is 624×10^{-6} (SI), ranging from 31×10^{-6} (SI) to 1527×10^{-6} (SI). The Flinn and P_j-T diagrams consistently show an oblate/prolate character in the distributions of the AMS principal axis. Positive correlations between bulk susceptibility and various rock magnetic properties (i.e., K_m versus NRM, K_m versus SIRM, and K_m versus M_s) suggest that susceptibility and remanence are carried by a common mineral, that is, authigenic magnetite.

The χ/χ_{ARM} ratio of the specimens indicates SD magnetite as the dominant magnetic carrier, while the Néel diagram reveals that the magnetite particles likely possess axial ratios <1.3:1, a crucial factor influencing magnetic anisotropy. The resulting inverse magnetic fabrics are attributed to these SD domain magnetite particles. The magnetic fabrics are categorized into four groups, and the K_1 axis of all four groups indicates a paleo-compression direction of NE-SW during the Eocene. Given the ~20° clockwise rotation of the study area relative to Eurasia since the Paleogene, we interpret that the AMS documented the NNE-SSW oriented compression during the remagnetization. It is noteworthy that previous research has documented an early Paleogene NE-SW compression in the Gongjue area. This inconsistency in compression patterns represents the early response to the India-Eurasia collision, resulting in subsequent oroclinal bending around the EHS.

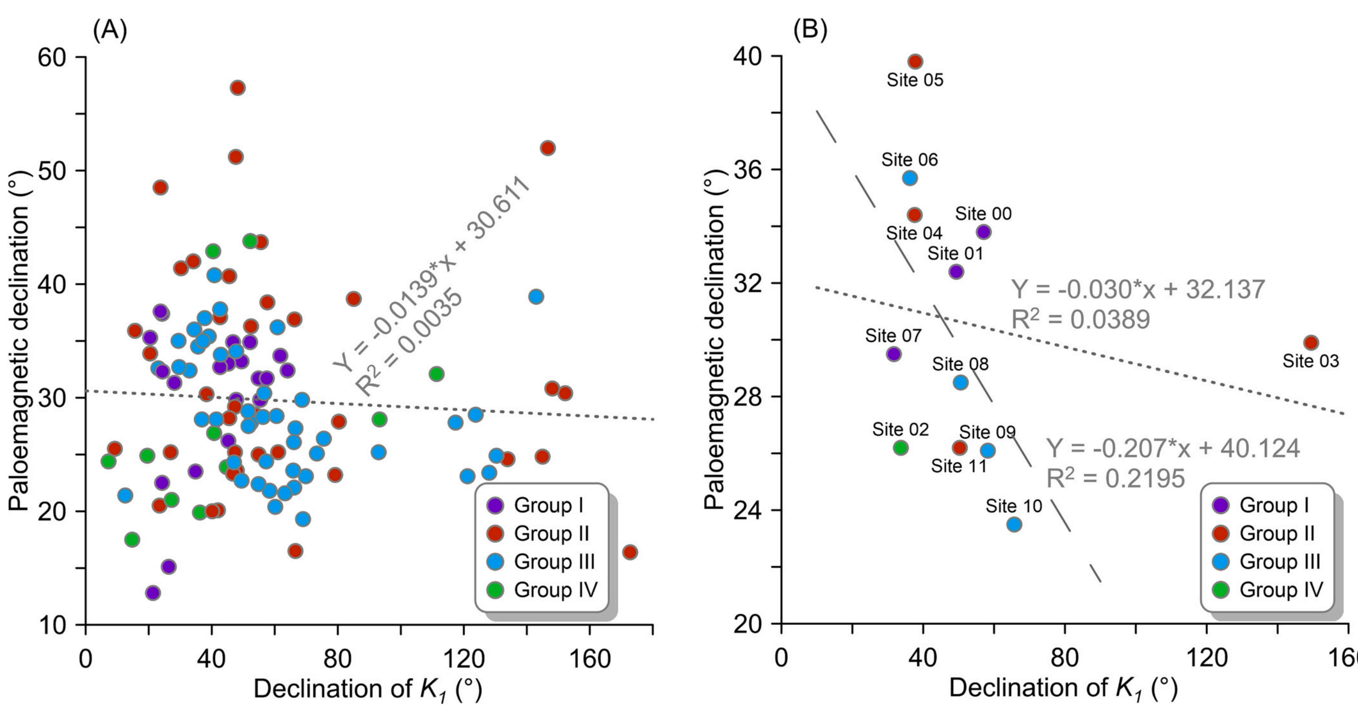

Fig. 12. Correlation diagram comparing the declination of K_1 to the paleomagnetic declination, shown for both (A) sample-level and (B) site-level analyses. The long-dashed line represents the fitted trend excluding site 3, while the short-dashed line encompasses all samples/sites.

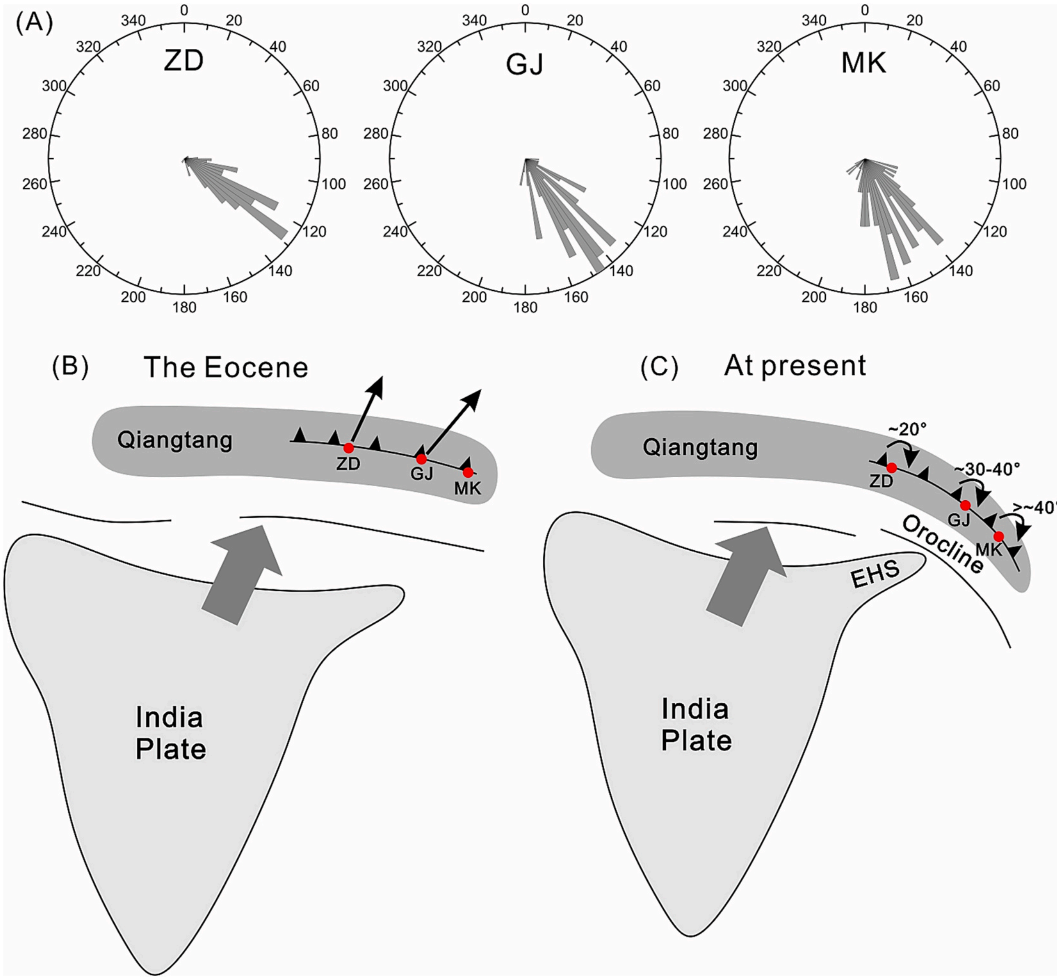

Fig. 13. (A). Rose diagrams of the fault strikes in the Zaduo (ZD), Gongjue (GJ) and Mangkang (MK) areas. (B) and (C). Schematic models illustrating (B) deformation of the Qiangtang Terrane in the Eocene and (C) evolution of the orocline after the late Eocene. The black arrows in (B) represent the compression directions in the Zaduo and Gongjue areas.

CRediT authorship contribution statement

Qiang Fu: Writing – original draft, Visualization, Methodology, Investigation, Formal analysis, Conceptualization. **Maodu Yan:** Writing – review & editing, Validation, Supervision, Methodology, Conceptualization. **Mark J. Dekkers:** Writing – review & editing, Validation, Supervision, Methodology, Conceptualization. **Bingshuai Li:** Investigation, Formal analysis. **Chong Guan:** Investigation, Formal analysis. **Liang Yu:** Investigation, Formal analysis. **Wanlong Xu:** Investigation, Formal analysis. **Miaomiao Shen:** Investigation, Formal analysis. **Zunbo Xu:** Investigation, Formal analysis.

Declaration of Competing Interest

The authors declare that they have no known competing financial interests or personal relationships that could have appeared to influence the work reported in this paper.

Data availability

Data will be made available on request.

Acknowledgments

The supporting data for our conclusions can be accessed in the supplementary materials. We thank the Editor Gideon Rosenbaum, reviewer S.H. Li, and the other anonymous reviewer for their constructive comments that greatly enhanced the manuscript. We thank Z.T. Feng for the assistance during field investigation, Jasper Maars for insightful discussions. This work is co-supported by the National Natural Science Foundation of China (Grants 41974080, 41988101-01), the National Key Research and Development Program of China (2022YFF0800502), the Second Tibetan Plateau Scientific Expedition and Research Grant (2019QZKK0707).

Appendix A. Supplementary data

Supplementary data to this article can be found online at https://doi.org/10.1016/j.tecto.2023.230175.

References

Aben, F.M., Dekkers, M.J., Bakker, R.R., van Hinsbergen, D.J.J., Zachariasse, W.J., Tate, G.W., et al., 2014. Untangling Inconsistent magnetic Polarity Records through an Integrated Rock magnetic Analysis: a Case Study on Neogene Sections in East Timor. Geochem. Geophys. Geosyst. 15, 2531–2554. https://doi.org/10.1002/2014gc005294.

Allmendinger, R.W., Cardozo, N., Fisher, D.M., 2011. Structural Geology Algorithms: Vectors and Tensors. Cambridge University Press, p. 289.

An, Z., Kutzbach, J.E., Prell, W.L., Porter, S.C., 2001. Evolution of Asian monsoons and phased uplift of the Himalaya–Tibetan plateau since Late Miocene times. Nature 411, 62–66. https://doi.org/10.1038/35075035.

Antolín-Tomás, B., Román-Berdiel, T., Casas-Sainz, A., Gil-Peña, I., Oliva, B., Soto, R., 2009. Structural and magnetic fabric study of the Marimanha granite (Axial Zone of the Pyrenees). Int. J. Earth Sci. 98, 427–441.

Aubourg, C., Rochette, P., Stéphan, J.F., Popoff, M., Chabert-Pelline, C., 1999. The magnetic fabric of weakly deformed late Jurassic shales from the southern subalpines chains (French Alps): evidence for SW-directed tectonic transport direction. Tectonophysics 307, 15–31.
Bascou, J., Camps, P., Dautria, J.M., 2005. Magnetic versus crystallographic fabrics in a basaltic lava flow. J. Volcanol. Geotherm. Res. 145, 119–135.
Beck, R.A., Burbank, D.W., Sercombe, W.J., Riley, G.W., Barndt, J.K., Berry, J.R., Afzal, J., Khan, A.M., Jurgen, H., Metje, J., 1995. Stratigraphic evidence for an early collision between Northwest India and Asia. Nature 373, 55–58.
Bilardello, D., 2021. Late Paleozoic depositional environments and sediment transport directions of the Itararé Group rocks from the state of São Paulo, Brazil, determined from rock magnetism and magnetic anisotropy. Earth and Space Sc. 8 e2021EA001703.
Blumstein, A.M., Elmore, R.D., Engel, M.H., Elliot, C., Basu, A., 2004. Paleomagnetic dating of burial diagenesis in Mississippian carbonates, Utah. J. Geophys. Res. Solid Earth 109.
Borradaile, G., 1987. Anisotropy of magnetic susceptibility: rock composition versus strain. Tectonophysics 138, 327–329.
Borradaile, G.J., 1988. Magnetic susceptibility, petrofabrics and strain. Tectonophysics 156, 1–20.
Borradaile, G.J., Jackson, M., 2010. Structural geology, petrofabrics and magnetic fabrics (AMS, AARM, AIRM). J. Struct. Geol. 32, 1519–1551.
Burchfiel, B., Quidong, D., Molnar, P., Royden, L., Yipeng, W., Peizhen, Z., Weiqi, Z., 1989. Intracrustal detachment within zones of continental deformation. Geology 17, 748–752.
Butler, R.F., 1992. Paleomagnetism: Magnetic Domains to Geologic Terranes, 319. Blackwell Scientific Publications Boston.
Calvín Ballester, P., Villalaín Santamaria, J.J., Casas-Sainz, A.M., 2018a. Anisotropic magnetite growth in remagnetized limestones: Tectonic constraints and implications for basin history. Geology 46, 751–754.
Calvín Ballester, P., Villalaín Santamaria, J.J., Casas Sainz, A.M., 2018b. The carriers of AMS in remagnetized carbonates. Insights for remagnetization mechanism and basin evolution. Phys. Earth Planet. Inter. 282, 1–20.
Cañón-Tapia, E., Mendoza-Borunda, R., 2014. Magnetic petrofabric of igneous rocks: Lessons from pyroclastic density current deposits and obsidians. J. Volcanol. Geotherm. Res. 289, 151–169.
Cao, X., Sun, Z., Li, H., Cao, Y., Huang, B., Wu, B., Ye, X., Liu, C., Yang, Z., Berndt, T.A., 2021. Cenozoic deformation in the Tethyan Himalaya, SE Tibet: Insights from magnetic fabrics and structural analysis of Upper Triassic flysch. Tectonophysics 814, 228967.
Cardozo, N., Allmendinger, R.W., 2013. Spherical projections with OSXStereonet. Comput. Geosci. 51, 193–205.
Chadima, M., Jelinek, V., 2009. Anisoft 4.2: Anisotropy Data Browser for Windows. Agico Inc., Brno.
Channell, J., McCabe, C., 1994. Comparison of magnetic hysteresis parameters of unremagnetized and remagnetized limestones. J. Geophys. Res. Solid Earth 99, 4613–4623.
Chen, H., Jon, D., Friedrich, H., Hao, J., 1995. Paleomagnetic evidence for clockwise rotation of the Simao region since the cretaceous: a consequence of India-Asia collision. Earth Planet. Sci. Lett. 134, 203–217.
Chen, Y., Li, W., Yuan, X., Badal, J., Teng, J., 2015. Tearing of the Indian lithospheric slab beneath southern Tibet revealed by SKS-wave splitting measurements. Earth Planet. Sci. Lett. 413, 13–24.
Cifelli, F., Mattei, M., Hirt, A., Günther, A., 2004. The origin of tectonic fabrics in "undeformed" clays: the early stages of deformation in extensional sedimentary basins. Geophys. Res. Lett. 31.
Cifelli, F., Mattei, M., Chadima, M., Hirt, A., Hansen, A., 2005. The origin of tectonic lineation in extensional basins: combined neutron texture and magnetic analyses on "undeformed" clays. Earth Planet. Sci. Lett. 235, 62–78.
Cifelli, F., Mattei, M., Chadima, M., Lenser, S., Hirt, A., 2009. The magnetic fabric in "undeformed clays": AMS and neutron texture analyses from the Rif Chain (Morocco). Tectonophysics 466, 79–88.
Dankers, P.H.M., 1978. Magnetic Properties of Dispersed Natural Iron-Oxides of Known Grain-Size. PhD thesis, 143. Rijksuniversiteit te Utrecht.
Ding, L., Maksatbek, S., Cai, F., Wang, H., Song, P., Ji, W., Xu, Q., Zhang, L., Muhammad, Q., Upendra, B., 2017. Processes of initial collision and suturing between India and Asia. Sci. China Earth Sci. 60, 635–651.
Ding, L., Kapp, P., Cai, F.L., Garzione, C.N., Xiong, Z.Y., Wang, H.Q., Wang, C., 2022. Timing and mechanisms of Tibetan Plateau uplift. Nat. Rev. Earth Environ. 3, 652–667.
Dunlop, D.J., 2002. Theory and application of the Day plot (Mrs/Ms versus Hcr/Hc) 2. Application to data for rocks, sediments, and soils. J. Geophys. Res. Solid Earth 107. EPM 5-1-EPM 5-15.
Ejembi, J.I., Ferré, E.C., Satolli, S., Friedman, S.A., 2020. Post-depositional fluid flow in Jurassic sandstones of the Uncompahgre Uplift: Insights from magnetic fabrics. Front. Earth Sci. 8, 601415.
England, P., Houseman, G., 1989. Extension during continental convergence, with application to the Tibetan Plateau. J. Geophys. Res. Solid Earth 94, 17561–17579.
Evans, M.A., Lewchuk, M., Elmore, R., 2003. Strain partitioning of deformation mechanisms in limestones: examining the relationship of strain and anisotropy of magnetic susceptibility (AMS). J. Struct. Geol. 25, 1525–1549.
Fabian, K., Von Dobeneck, T., 1997. Isothermal magnetization of samples with stable Preisach function: a survey of hysteresis, remanence, and rock magnetic parameters. J. Geophys. Res. Solid Earth 102, 17659–17677.
Fang, X., Song, C., Yan, M., Zan, J., Liu, C., Sha, J., Zhang, W., Zeng, Y., Wu, S., Zhang, D., 2016. Mesozoic litho-and magneto-stratigraphic evidence from the central Tibetan Plateau for megamonsoon evolution and potential evaporites. Gondwana Res. 37, 110–129.
Ferré, E.C., 2002. Theoretical models of intermediate and inverse AMS fabrics. Geophys. Res. Lett. 29, 31-31-31-34.
Flinn, D., 1965. On the symmetry principle and the deformation ellipsoid. Geol. Mag. 102, 36–45.
Font, E., Trindade, R.I.F., Nédélec, A., 2006. Remagnetization in bituminous limestones of the Neoproterozoic Araras Group (Amazon craton): Hydrocarbon maturation, burial diagenesis, or both? J. Geophys. Res. Solid Earth 111, B06204. https://doi.org/10.1029/2005JB004106.
Fu, Q., Yan, M., Dekkers, M.J., Guan, C., Yu, L., Xu, W., Li, B., Feng, Z., Xu, Z., Shen, M., 2022. Remagnetization of the Jurassic Limestones in the Zaduo Area, Eastern Qiangtang Terrane (Tibetan Plateau, China): Implications for the India-Eurasia collision. Geophys. J. Int.Volume 228, 2073–2091. https://doi.org/10.1093/gji/ggab402.
Fuller, M.D., 1963. Magnetic anisotropy and paleomagnetism. J. Geophys. Res. 68, 293–309.
Fuller, M., 1969. Magnetic orientation of borehole cores. Geophysics 34, 772–774.
Gao, L., Yang, Z., Tong, Y., Wang, H., An, C., 2015. New paleomagnetic studies of Cretaceous and Miocene rocks from Jinggu, western Yunnan, China: Evidence for internal deformation of the Lanping–Simao Terrane. J. Geodyn. 89, 39–59.
García-Lasanta, C., Oliva-Urcia, B., Román-Berdiel, T., Casas, A., Gil-Peña, I., Sánchez-Moya, Y., Sopeña, A., Hirt, A., Mattei, M., 2015. Evidence for the Permo-Triassic transtensional rifting in the Iberian Range (NE Spain) according to magnetic fabrics results. Tectonophysics 651, 216–231.
García-Lasanta, C., Oliva-Urcia, B., Casas-Sainz, A., Román-Berdiel, T., Izquierdo-Llavall, E., Soto, R., Calvín, P., Moussaid, B., El Ouardi, H., Kullberg, J., 2018. Inversion tectonics and magnetic fabrics in Mesozoic basins of the Western Tethys: a review. Tectonophysics 745, 1–23.
Hargraves, R.B., Fischer, A.G., 1959. Remanent magnetism in Jurassic red limestones and radiolarites from the Alps. Geophys. J. Int. 2, 34–41.
Hoke, G.D., Liu-Zeng, J., Hren, M.T., Wissink, G.K., Garzione, C.N., 2014. Stable isotopes reveal high southeast Tibetan Plateau margin since the Paleogene. Earth Planet. Sci. Lett. 394, 270–278.
Horton, B.K., Yin, A., Spurlin, M.S., Zhou, J., Wang, J., 2002. Paleocene–Eocene syncontractional sedimentation in narrow, lacustrine-dominated basins of east-central Tibet. Geol. Soc. Am. Bull. 114, 771–786.
Hou, Z., Zhang, H., 2015. Geodynamics and metallogeny of the eastern Tethyan metallogenic domain. Ore Geol. Rev. 70, 346–384.
Hou, Z., Zaw, K., Pan, G., Mo, X., Xu, Q., Hu, Y., Li, X., 2007. Sanjiang Tethyan metallogenesis in SW China: Tectonic setting, metallogenic epochs and deposit types. Ore Geol. Rev. 31, 48–87.
Hounslow, M., 1985. Magnetic fabric arising from paramagnetic phyllosilicate minerals in mudrocks. J. Geol. Soc. Lond. 142, 995–1006.
Hrouda, F., 1982. Magnetic anisotropy of rocks and its application in geology and geophysics. Geophys. Surv. 5, 37–82.
Hrouda, F., Jelinek, V., 1990. Resolution of ferrimagnetic and paramagnetic anisotropies in rocks, using combined low-field and high-field measurements. Geophys. J. Int. 103, 75–84.
Huang, K., Opdyke, N.D., Li, J., Peng, X., 1992. Paleomagnetism of cretaceous rocks from eastern Qiangtang terrane of Tibet. J. Geophys. Res. Solid Earth 97, 1789–1799.
Jackson, M., 1991. Anisotropy of magnetic remanence: a brief review of mineralogical sources, physical origins, and geological applications, and comparison with susceptibility anisotropy. Pure Appl. Geophys. 136, 1–28.
Jackson, M., Swanson-Hysell, N.L., 2012. Rock magnetism of remagnetized carbonate rocks: another look. Geol. Soc. Lond. Spec. Publ. 371, 229–251.
Jelínek, V., 1977. The Statistical Theory of Measuring Anisotropy of Magnetic Susceptibility of Rocks and its Application. Geofyzika Brno, Czech Republic.
Jelinek, V., 1981. Characterization of the magnetic fabric of rocks. Tectonophysics 79, T63–T67.
Jelínek, V., Kropáček, V., 1978. Statistical processing of anisotropy of magnetic susceptibility measured on groups of specimens. Stud. Geophys. Geod. 22, 50–62.
Jiang, K., Liang, W., Wu, G., Liu, C., Zou, X., He, X., Li, J., Wang, X., Zheng, B., Shen, Q., 2022. Anisotropy of magnetic susceptibility Study and its significance in the Late Cretaceous-Cenozoic Sanmenxia Basin in the southeastern shanxi rift, Central China. Solid Earth Sci. 7, 135–150. https://doi.org/10.1016/j.sesci.2022.02.002.
Kapp, P., Yin, A., Harrison, T.M., Ding, L., 2005. Cretaceous-Tertiary shortening, basin development, and volcanism in Central Tibet. Geol. Soc. Am. Bull. 117, 865–878.
Kars, M., Aubourg, C., Labaume, P., Berquó, T.S., Cavailhes, T., 2014. Burial diagenesis of magnetic minerals: New insights from the Grès d'Annot Transect (SE France). Minerals 4, 667–689.
Katz, B., Elmore, R.D., Cogoini, M., Engel, M.H., Ferry, S., 2000. Associations between burial diagenesis of smectite, chemical remagnetization, and magnetite authigenesis in the Vocontian trough, SE France. J. Geophys. Res. Solid Earth 105 (B1), 851–868.
Kondo, K., Mu, C., Yamamoto, T., Zaman, H., Miura, D., Yokoyama, M., Ahn, H.-S., Otofuji, Y.-I., 2012. Oroclinal origin of the Simao Arc in the Shan-Thai Block inferred from the cretaceous palaeomagnetic data. Geophys. J. Int. 190, 201–216.
Kornfeld, D., Eckert, S., Appel, E., Ratschbacher, L., Pfänder, J., Liu, D., Ding, L., 2014. Clockwise rotation of the Baoshan Block due to southeastward tectonic escape of Tibetan crust since the Oligocene. Geophys. J. Int. 197, 149–163.
Larrasoaña, J.C., Pueyo, E.L., Parés, J.M., 2004. An integrated AMS, structural, palaeo- and rock-magnetic study of Eocene marine marls from the Jaca-Pamplona basin (Pyrenees, N Spain); new insights into the timing of magnetic fabric acquisition in weakly deformed mudrocks. Geol. Soc. Lond. Spec. Publ. 238, 127–143.

Leloup, P.H., Lacassin, R., Tapponnier, P., Schärer, U., Zhong, D., Liu, X., Zhang, L., Ji, S., Trinh, P.T., 1995. The Ailao Shan-Red river shear zone (Yunnan, China), tertiary transform boundary of Indochina. Tectonophysics 251, 3–84.
Li, C., 1987. The Longmucuo-Shuanghu-Lancangjiang plate suture and the north boundary of distribution of Gondwana facies Permo-Carboniferous system in northern Xizang, China. J. Changchun Coll. Geol. 17, 155–166.
Li, H., Zhang, S., 2005. Detection of mineralogical changes in pyrite using measurements of temperature-dependence susceptibilities. Chin. J. Geophys. 48, 1454–1461.
Li, C., Zhai, G., Wang, L., Yin, F., Mao, X., 2009. An important window for understanding the Qinghai–Tibet Plateau—a review on research progress in recent years of Qiangtang area, Tibet, China. Geol. Bull. China 28, 1169–1177.
Li, S., Yang, Z., Deng, C., He, H., Qin, H., Sun, L., Yuan, J., van Hinsbergen, D.J., Krijgsman, W., Dekkers, M.J., 2017. Clockwise rotations recorded in redbeds from the Jinggu Basin of northwestern Indochina. GSA Bull. 129, 1100–1122.
Li, L., Fan, M., Davila, N., Jesmok, G., Mitsunaga, B., Tripati, A., Orme, D., 2019. Carbonate stable and clumped isotopic evidence for late Eocene moderate to high elevation of the east-central Tibetan Plateau and its geodynamic implications. GSA Bull. 131, 831–844.
Li, B., Yan, M., Zhang, W., Parés, J.M., Fang, X., Yang, Y., Zhang, D., Guan, C., Bao, J., 2020a. Magnetic fabric constraints on the cenozoic compressional strain changes in the northern qaidam marginal thrust belt and their tectonic implications. Tectonics 39 e2019TC005989.
Li, S., van Hinsbergen, D.J., Najman, Y., Liu, Z.J., Deng, C., Zhu, R., 2020b. Does pulsed Tibetan deformation correlate with Indian plate motion changes? Earth Planet. Sci. Lett. 536, 116144.
Li, S., van Hinsbergen, D.J., Shen, Z., Najman, Y., Deng, C., Zhu, R., 2020c. Anisotropy of magnetic susceptibility (AMS) analysis of the Gonjo Basin as an independent constraint to date Tibetan shortening pulses. Geophys. Res. Lett. 47 e2020GL087531.
Li, B., Yan, M., Zhang, W., Fang, X., Yang, Y., Zhang, D., Guan, C., Bao, J., 2021. Two-stage strike-slip faulting of the Altyn Tagh Fault revealed by magnetic fabrics in the Qaidam Basin. Tectonophysics 821, 229142.
Lippert, P.C., Zhao, X., Coe, R.S., Lo, C., 2011. Palaeomagnetism and 40Ar/39Ar geochronology of upper Palaeogene volcanic rocks from Central Tibet: implications for the Central Asia inclination anomaly, the palaeolatitude of Tibet and post-50 Ma shortening within Asia. Geophys. J. Int. 184, 131–161.
Liu, Q., Banerjee, S.K., Jackson, M.J., Maher, B.A., Pan, Y., Zhu, R., Chen, F., 2004. Grain sizes of susceptibility and anhysteretic remanent magnetization carriers in Chinese loess/paleosol sequences. J. Geophys. Res. Solid Earth 109 (B3).
Lowrie, W., Heller, F., 1982. Magnetic properties of marine limestones. Rev. Geophys. 20, 171–192.
Lüneburg, C.M., Lampert, S.A., Lebit, H.D., Hirt, A.M., Casey, M., Lowrie, W., 1999. Magnetic anisotropy, rock fabrics and finite strain in deformed sediments of SW Sardinia (Italy). Tectonophysics 307, 51–74.
Luo, L., Jia, D., Li, H., Li, Y., Deng, F., Chen, Z., Jia, Q., Sun, S., Zhang, Y., 2009. Magnetic fabric investigation in the northwestern Sichuan Basin and its regional inference. Phys. Earth Planet. Inter. 173, 103–114.
Luo, L., Qi, J.F., Jia, D., Wang, K., Zeng, X., 2013. Magnetic fabric investigation in Tianquan-Leshan section in front of Longmenshan fold-thrust belt and its indicative significance for the Cenozoic deformation. Chin. J. Geophys. 56, 558–566 (in Chinese with English abstract).
Maher, B.A., 1988. Magnetic properties of some synthetic sub-micron magnetites. Geophys. J. Int. 94 (1), 83–96.
Mattei, M., Sagnotti, L., Faccenna, C., Funiciello, R., 1997. Magnetic fabric of weakly deformed clay-rich sediments in the Italian peninsula: relationship with compressional and extensional tectonics. Tectonophysics 271, 107–122.
Metcalfe, I., 2013. Gondwana dispersion and Asian accretion: Tectonic and palaeogeographic evolution of eastern Tethys. J. Asian Earth Sci. 66, 1–33.
Molnar, P., Tapponnier, P., 1975. Cenozoic Tectonics of Asia: Effects of a Continental Collision: Features of recent continental tectonics in Asia can be interpreted as results of the India-Eurasia collision. Science 189, 419–426.
Mullender, T., Van Velzen, A., Dekkers, M., 1993. Continuous drift correction and separate identification of ferrimagnetic and paramagnetic contributions in thermomagnetic runs. Geophys. J. Int. 114, 663–672.
Néel, L., 1955. Some theoretical aspects of rock-magnetism. Adv. Phys. 4, 191–243.
Oliva-Urcia, B., Larrasoaña, J., Pueyo, E., Gil, A., Mata, P., Parés, J., Schleicher, A.M., Pueyo, O., 2009. Disentangling magnetic subfabrics and their link to deformation processes in cleaved sedimentary rocks from the Internal Sierras (west Central Pyrenees, Spain). J. Struct. Geol. 31, 163–176.
Oliva-Urcia, B., Rahl, J.M., Schleicher, A.M., Parés, J.M., 2010. Correlation between the anisotropy of the magnetic susceptibility, strain and X-ray Texture Goniometry in phyllites from Crete, Greece. Tectonophysics 486, 120–131.
Oliva-Urcia, B., Casas, A., Soto, R., Villalaín, J., Kodama, K., 2011. A transtensional basin model for the Organyà basin (central southern Pyrenees) based on magnetic fabric and brittle structures. Geophys. J. Int. 184, 111–130.
Oliva-Urcia, B., Román-Berdiel, T., Casas, A.M., Bógalo, M.F., Osácar, M.C., García-Lasanta, C., 2013. Transition from extensional to compressional magnetic fabrics in the cretaceous Cabuérniga basin (North Spain). J. Struct. Geol. 46, 220–234.
Özdemir, Ö., Banerjee, S.K., 1982. A preliminary magnetic study of soil samples from west-Central Minnesota. Earth Planet. Sci. Lett. 59 (2), 393–403.
Pan, G., Ding, J., Yao, D., Wang, L., 2004. Guidebook of 1: 1,500,000 Geologic map of the Qinghai–Xizang (Tibet) Plateau and Adjacent Areas. Chengdu Cartographic Publishing House, Chengdu, China, p. 48.
Parés, J.M., 2004. How deformed are weakly deformed mudrocks? Insights from magnetic anisotropy. Geol. Soc. Lond. Spec. Publ. 238, 191–203.
Passier, H.F., de Lange, G.J., Dekkers, M.J., 2001. Magnetic properties and geochemistry of the active oxidation front and the youngest sapropel in the eastern Mediterranean Sea. Geophys. J. Int. 145, 604–614.
Potter, D.K., Stephenson, A., 1988. Single-domain particles in rocks and magnetic fabric analysis. Geophys. Res. Lett. 15, 1097–1100.
Pueyo Anchuela, Ó., Ramajo Cordero, J., Gil Imaz, A., Meléndez Hevia, G., 2013. Analysis of anisotropy of magnetic susceptibility in iron-oolitic beds: a potential tool for paleocurrent identification. Int. J. Earth Sci. 102, 1131–1149.
Pusok, A.E., Stegman, D.R., 2020. The convergence history of India-Eurasia records multiple subduction dynamics processes. Sci. Adv. 6, eaaz8681.
Qinghai Geological Survey Institute (QGSI), 2005. Geological Map (1:250000) of the People's Republic of China-Zaduo County Sheet. China University of Geosciences Press (in Chinese).
Qinghai Geological Survey Institute (QGSI), 2014. 1:250000 Geological Survey Report of the People's Republic of China-Zaduo County sheet. China University of Geosciences Press (in Chinese). ISBN: 9787562533832).
Raymo, M.E., Ruddiman, W.F., 1992. Tectonic forcing of late Cenozoic climate. nature 359, 117–122.
Replumaz, A., Tapponnier, P., 2003. Reconstruction of the deformed collision zone between India and Asia by backward motion of lithospheric blocks. J. Geophys. Res. Solid Earth 108.
Roberts, A.P., Tauxe, L., Heslop, D., Zhao, X., Jiang, Z., 2018. A critical appraisal of the "Day" diagram. J. Geophys. Res. Solid Earth 123, 2618–2644.
Rochette, P., 1987a. Magnetic susceptibility of the rock matrix related to magnetic fabric studies. J. Struct. Geol. 9, 1015–1020.
Rochette, P., 1987b. Metamorphic control of the magnetic mineralogy of black shales in the Swiss Alps: toward the use of "magnetic isogrades". Earth Planet. Sci. Lett. 84, 446–456.
Rochette, P., 1988. Inverse magnetic fabric in carbonate-bearing rocks. Earth Planet. Sci. Lett. 90, 229–237.
Rochette, P., Jackson, M., Aubourg, C., 1992. Rock magnetism and the interpretation of anisotropy of magnetic susceptibility. Rev. Geophys. 30, 209–226.
Roperch, P., Dupont-Nivet, G., Guillot, S., Goussin, F., Huang, W., Replumaz, A., Yang, Z., Guo, Z., Song, B., 2017. Paleomagnetic constraints on early collisional deformation along the eastern margin of the Qiantang terrane (Tibetan plateau) at 50 and 37 Ma. In: EGU General Assembly Conference Abstracts, p. 9476.
Royden, L.H., Burchfiel, B.C., King, R.W., Wang, E., Chen, Z.L., Shen, F., Liu, Y.P., 1997. Surface deformation and lower crustal flow in eastern Tibet. Science 276 (5313), 788–790.
Royden, L.H., Burchfiel, B.C., van der Hilst, R.D., 2008. The geological evolution of the Tibetan Plateau. science 321, 1054–1058.
Ruddiman, W.F., Kutzbach, J.E., 1989. Forcing of late Cenozoic northern hemisphere climate by plateau uplift in southern Asia and the American West. J. Geophys. Res. Atmos. 94, 18409–18427.
Saint-Bezar, B., Hebert, R., Aubourg, C., Robion, P., Swennen, R., De Lamotte, D.F., 2002. Magnetic fabric and petrographic investigation of hematite-bearing sandstones within ramp-related folds: examples from the South Atlas Front (Morocco). J. Struct. Geol. 24, 1507–1520.
Sato, K., Liu, Y., Wang, Y., Yokoyama, M., Yoshioka, S.Y., Yang, Z., Otofuji, Y.-I., 2007. Paleomagnetic study of cretaceous rocks from Pu'er, western Yunnan, China: evidence of internal deformation of the Indochina block. Earth Planet. Sci. Lett. 258, 1–15.
Song, C., Zeng, Y., Yan, M., Wu, S., Fang, X., Bao, J., Zan, J., Liu, X., 2016. Magnetostratigraphy of the middle-upper Jurassic sedimentary sequences at Yanshiping, Qiangtang Basin, China. Geophys. J. Int. 206, 1847–1863.
Su, T., Spicer, R.A., Li, S.H., Xu, H., Huang, J., Sherlock, S., Huang, Y.J., Li, S.F., Wang, L., Jia, L.B., 2019. Uplift, climate and biotic changes at the Eocene–Oligocene transition in south-eastern Tibet. Natl. Sci. Rev. 6, 495–504.
Su, T., Spicer, R.A., Wu, F.X., Farnsworth, A., Huang, J., Del Rio, C., Zhou, Z.K., 2020. A Middle Eocene lowland humid subtropical "Shangri-La" ecosystem in Central Tibet. Proc. Natl. Acad. Sci. 117, 32989–32995.
Suk, D., van der Voo, R., Peacor, D.R., 1993. Origin of magnetite responsible for remagnetization of early Paleozoic limestones of New York State. J. Geophys. Res. Solid Earth 98, 419–434.
Sun, W., Jackson, M., Craddock, J.P., 1993. Relationship between remagnetization, magnetic fabric and deformation in Paleozoic carbonates. Tectonophysics 221, 361–366.
Tanaka, K., Mu, C., Sato, K., Takemoto, K., Miura, D., Liu, Y., Zaman, H., Yang, Z., Yokoyama, M., Iwamoto, H., Uno, K., Otofuji, Y.-I., 2008. Tectonic deformation around the eastern Himalayan syntaxis: constraints from the cretaceous palaeomagnetic data of the Shan-Thai Block. Geophys. J. Int. 175, 713–728.
Tang, Z., Dong, X., Wang, X., Ding, Z., 2015. Oligocene-M iocene magnetostratigraphy and magnetic anisotropy of the B axbulak section from the P amir-T ian S han convergence zone. Geochem. Geophys. Geosyst. 16, 3575–3592.
Tang, M., Liu, Z.J., Hoke, G.D., Xu, Q., Wang, W., Li, Z., Zhang, J., Wang, W., 2017. Paleoelevation reconstruction of the Paleocene-Eocene Gonjo basin, SE-central Tibet. Tectonophysics 712-713, 170–181.
Tapponnier, P., Lacassin, R., Leloup, P.H., Schärer, U., Dalai, Z., Haiwei, W., Xiaohan, L., Shaocheng, J., Lianshang, Z., Jiayou, Z., 1990. The Ailao Shan/Red River metamorphic belt: tertiary left-lateral shear between Indochina and South China. Nature 343, 431–437.
Tapponnier, P., Zhiqin, X., Roger, F., Meyer, B., Arnaud, N., Wittlinger, G., Jingsui, Y., 2001. Oblique stepwise rise and growth of the Tibet Plateau. Science 294, 1671–1677.
Tarling, D., Hrouda, F., 1993. Agnetic Anisotropy of Rocks. Springer Science & Business Media.

Tauxe, L., 2010. Essentials of Paleomagnetism. Univ of California Press, p. 126.
Tauxe, L., Bertram, H.N., Seberino, C., 2002. Physical interpretation of hysteresis loops: Micromagnetic modeling of fine particle magnetite. Geochem. Geophys. Geosyst. 3, 1–22.
Todrani, A., Speranza, F., D`Agostino, N., Zhang, B., 2022. Post-50 Ma Evolution of India-Asia Collision Zone from Paleomagnetic and GPS Data: Greater India Indentation to Eastward Tibet Flow. Geophys. Res. Lett. 49 e2021GL096623.
Tong, Y., Yang, Z., Zheng, L., Xu, Y., Wang, H., Gao, L., Hu, X., 2013. Internal crustal deformation in the northern part of Shan-Thai Block: New evidence from paleomagnetic results of cretaceous and Paleogene redbeds. Tectonophysics 608, 1138–1158.
Tong, Y., Yang, Z., Gao, L., Wang, H., Zhang, X., An, C., Xu, Y., Han, Z., 2015. Paleomagnetism of Upper Cretaceous red-beds from the eastern Qiangtang Block: Clockwise rotations and latitudinal translation during the India–Asia collision. J. Asian Earth Sci. 114, 732–749.
Tong, Y., Yang, Z., Mao, C., Pei, J., Pu, Z., Xu, Y., 2017. Paleomagnetism of Eocene red-beds in the eastern part of the Qiangtang Terrane and its implications for uplift and southward crustal extrusion in the southeastern edge of the Tibetan Plateau. Earth Planet. Sci. Lett. 475, 1–14.
Tong, Y., Yang, Z., Pei, J., Wang, H., Wu, Z., Li, J., 2022. Upper Crustal Collapse Reconstructed the Topography and Remodeled the Fault System of the Chuandian Fragment in the Southeastern Edge of the Tibetan Plateau, Evidenced by Anisotropy of magnetic Susceptibility Data Sets. Tectonics 41 e2021TC007126.
van Hinsbergen, D.J., Steinberger, B., Doubrovine, P.V., Gassmöller, R., 2011. Acceleration and deceleration of India-Asia convergence since the cretaceous: Roles of mantle plumes and continental collision. J. Geophys. Res. Solid Earth 116.
Wang, M., Shen, Z.K., 2020. Present-day crustal deformation of continental China derived from GPS and its tectonic implications. J. Geophys. Res. Solid Earth 125 e2019JB018774.
Wang, L., Pan, Y., Li, J., Qin, H., 2008. Magnetic properties related to thermal treatment of pyrite. Sci. China Ser. D Earth Sci. 51, 1144–1153.
Wang, K., Jia, D., Luo, L., Dong, S., 2017. Magnetic fabric and structural deformation. Chin. J. Geophys. 60, 1007–1026.
Weil, A.B., Yonkee, A., 2009. Anisotropy of magnetic susceptibility in weakly deformed red beds from the Wyoming salient, Sevier thrust belt: Relations to layer-parallel shortening and orogenic curvature. Lithosphere 1, 235–256.
Winklhofer, M., Fabian, K., Heider, F., 1997. Magnetic blocking temperatures of magnetite calculated with a three-dimensional micromagnetic model. J. Geophys. Res. Solid Earth 102, 22695–22709.
Wu, F., Fang, X., Yang, Y., Dupont-Nivet, G., Nie, J., Fluteau, F., Han, W., 2022. Reorganization of Asian climate in relation to Tibetan Plateau uplift. Nat. Rev. Earth & Environ. 3 (10), 684–700.
Xiao, R., Zheng, Y., Liu, X., Yang, Q., Liu, G., Xia, L., Bian, Z., Guan, J., Feng, P., Xu, H., 2021. Synchronous Sedimentation in Gonjo Basin, Southeast Tibet in Response to India-Asia Collision Constrained by Magnetostratigraphy. Geochem. Geophys. Geosyst. 22 e2020GC009411.
Xiong, Z., Ding, L., Spicer, R.A., Farnsworth, A., Wang, X., Valdes, P.J., Su, T., Zhang, Q., Zhang, L., Cai, F., 2020. The early Eocene rise of the Gonjo Basin, SE Tibet: from low desert to high forest. Earth Planet. Sci. Lett. 543, 116312.
Yan, M., Zhang, D., Fang, X., Ren, H., Zhang, W., Zan, J., Song, C., Zhang, T., 2016. Paleomagnetic data bearing on the Mesozoic deformation of the Qiangtang Block: Implications for the evolution of the Paleo-and Meso-Tethys. Gondwana Res. 39, 292–316.
Xizang Geological Survey, 2007. Geological Map (1:250000) of the People's Republic of China-Mangkang Country Sheet. China University of Geosciences Press, Wuhan (in Chinese).
Yan, Y., Chen, L., Huang, B., Yi, Z., Zhao, J., 2019. Magnetic fabric constraint on tectonic setting of Paleoproterozoic dyke swarms in the North China Craton, China. Precambrian Res. 329, 247–261.
Yang, Z., Besse, J., 1993. Paleomagnetic study of Permian and Mesozoic sedimentary rocks from Northern Thailand supports the extrusion model for Indochina. Earth Planet. Sci. Lett. 117, 525–552.
Yang, Z., Yin, J., Sun, Z., Otofuji, Y.I., Sato, K., 2001. Discrepant cretaceous paleomagnetic poles between Eastern China and Indochina: a consequence of the extrusion of Indochina. Tectonophysics 334, 101–113.
Yin, A., Harrison, T.M., 2000. Geologic evolution of the Himalayan-Tibetan orogen. Annu. Rev. Earth Planet. Sci. 28, 211–280.
Yu, X., Huang, B., Guan, S., Fu, S., Cheng, F., Cheng, X., Zhang, T., Guo, Z., 2014. Anisotropy of magnetic susceptibility of Eocene and Miocene sediments in the Qaidam Basin, Northwest China: Implication for Cenozoic tectonic transition and depocenter migration. Geochem. Geophys. Geosyst. 15, 2095–2108.
Zhang, Y., Huang, W., Huang, B., van Hinsbergen, D.J., Yang, T., Dupont-Nivet, G., Guo, Z., 2018. 53–43 Ma deformation of eastern Tibet revealed by three stages of tectonic rotation in the Gongjue basin. J. Geophys. Res. Solid Earth 123, 3320–3338.
Zhang, W., Fang, X., Zhang, T., Song, C., Yan, M., 2020. Eocene rotation of the northeastern central Tibetan Plateau indicating stepwise compressions and eastward extrusions. Geophys. Res. Lett. 47 e2020GL088989.
Zhu, D.C., Zhao, Z.D., Niu, Y.L., Dilek, Y., Hou, Z.Q., Mo, X.X., 2013. The origin and pre-Cenozoic evolution of the Tibetan Plateau. Gondwana Res. 23, 1429–1454.
Zhu, D.C., Li, S.M., Cawood, P.A., Wang, Q., Zhao, Z.D., Liu, S.A., Wang, L.Q., 2016. Assembly of the Lhasa and Qiangtang terranes in Central Tibet by divergent double subduction. Lithos 245, 7–17.